



A state-dependent hyperelastic-plastic constitutive model considering shear-induced particle breakage in granular soils

Nazanin Irani^{1,2} · Ali Lashkari¹ · Merita Tafli² · Torsten Wichtmann²

Received: 26 July 2021 / Accepted: 28 June 2022 / Published online: 30 July 2022
© The Author(s) 2022

Abstract

An elastic–plastic constitutive model considering particle breakage for simulation of crushable granular soils behavior is proposed. In the model, elastic strain rates are derived from a modified Helmholtz free energy function, and the influence of plastic shear work-induced particle breakage on the elastic properties of sand is taken into account as an elastic–plastic coupling mechanism. A stress ratio-driven mechanism is employed for calculation of the plastic strain rates. The proposed model is capable of tracking the evolution of the grain size distribution (GSD) due to shear-induced particle breakage. The evolving breakage index of Einav (2007) (J Mech Phys Solids 55(6):1274–1297, 2007) is interrelated to the plastic shear work to avoid overestimation of shear-induced particle breakage in loose sands. A direct comparison between the model simulations and laboratory data has been carried out for five series of drained/undrained monotonic and cyclic triaxial tests covering a wide range of initial states. For the sake of comparison, predicted behaviors from a hypoplastic constitutive model specially developed for crushable granular soils are also included. It is shown that the proposed constitutive model can provide reasonable predictions using a single set of parameters for each series of the laboratory data.

Keywords Back-stress ratio · Crushable granular soils · Elastoplasticity theory · Elastic–plastic coupling · Hyperelasticity · Particle breakage

1 Introduction

Particle breakage plays a profound role in granular soils behavior [21, 35, 46, 87, 114, 127] which occurs under both high effective stress levels caused by construction of dams, pile installations, or high embankment, and under relatively low stress conditions for granular materials with weak grains such as carbonate sands, weathered soils, and rockfill materials [45, 47, 54, 72, 73, 76, 104, 117, 119, 129]. Previous experiments denote that the particle breakage in granular soils can be affected by a number of factors, including individual grain strength [35, 59], grain morphology [11, 55, 125], grain size distribution (GSD)

[27, 34, 65, 74, 105], magnitude of the imposed effective stresses [80, 87, 122], load duration [9, 103, 129], total strain and axial strain rate [15], drainage condition and degree of saturation [8, 76, 79], and soil relative density [44, 57, 93].

Particle breakage results in permeability reduction around perforations [26, 85], increase in the settlement of rockfill dams [1], creep in piles embedded in sands [68], reduction in the drained peak friction angle [6, 7, 46], rapid long-runout motion of landslides [83] and plays a fundamental role in stress–strain behavior of brittle granular soils [87, 104, 108, 114]. In the past, a wide spectrum of experimental studies has been conducted to investigate the effect of particle breakage on the location of the critical state line (CSL) in crushable granular soils. According to the findings, in the presence of particle breakage, the critical state is reached at lower void ratios [3, 30, 48, 57, 78, 101, 120, 126].

There exist two foremost traditions to consider particle breakage in constitutive models for granular soils: (i) modification of yield surface, dilatancy, plastic

✉ Nazanin Irani
n.irani@sutech.ac.ir

¹ Department of Civil and Environmental Engineering, Shiraz University of Technology, Shiraz, Iran

² Chair of Soil Mechanics, Foundation Engineering and Environmental Geotechnics, Ruhr-University, Bochum, Germany

hardening and enabling the possibility of non-unique CSL through introduction of elegant breakage-dependent free energy and energy dissipation functions e.g., [14, 22, 23, 81, 101], and (ii) phenomenological methods using breakage-driven relocation of CSL in the e vs. p' plane in conjunction with critical state compatible state-dependent constitutive equations e.g., [19, 39, 47, 69, 109, 115, 118, 121]. The former clever route guarantees thermodynamics consistency, however, its rich conceptual theoretical mechanics/mathematics corroborates some researchers prefer adoption of the second, but commonly simpler method. For instance, Einav [22, 23] introduced the theory of breakage mechanics with the purpose of modeling the behavior of crushable granular material from micro-mechanical considerations within the framework of hyperplasticity, guaranteeing thermodynamical consistency. Some studies extended the theory of breakage mechanics by connecting energetics with the micromechanics and investigating the variation of permeability in cataclastic zones [81], with inclusion of porosity as a state variable [90] and combined it with the Cosserat continuum through an elastic upscaling incorporating Cosserat state variables [14]. Tengattini et al. [101] introduced a porosity-dependent extension to the theory of [22, 23] wherein the critical state is predicted in an unforced natural way, rather than imposed a priori. Tengattini et al. [101] succeeded to derive yield function and dilatancy from the rate of dissipation, but accurate simulation of stress-softening behavior is still lacking [12]. The large tear drop-shaped yield function, the lack of kinematic hardening, and the absence of the state parameter of Been and Jefferies [4] as a simple, but effective means for distinction of the dense from loose states, and the lack of phase transformation e.g., Ishihara et al. [50] for modeling of initial contraction prior of the subsequent dilation in medium-dense and dense sand subjected to undrained shear prompt the requirement of coupling between hyperelasticity and the bounding surface plasticity for crushable soils.

A constitutive model in a hyperelastic-plastic frame for crushable granular materials is suggested here. Owing to simplicity of the basic constitutive equations, versatility in simulation of various aspects of the mechanical behavior of granular soils, clear physical meaning of the parameters in one hand and ease of calibration using both data of monotonic and cyclic tests on the other, the state-dependent bounding surface model proposed by Dafalias and Manzari [16] has been adopted as benchmark to establish a hyperelastic-plastic constitutive model for crushable granular soils. A generalized Jiang and Liu [52]-type Helmholtz free energy function has been employed to derive elastic strain rates as well as the pressure-dependent soil elastic moduli. Hyperplastic theories for the granular soils with pressure-dependent moduli can take into account stress-

induced anisotropy of the elastic response in a natural unforced way and improve model predictions under cyclic loading e.g., [24, 31, 38]. A breakage index depending on plastic shear work (say function of shear stress and plastic shear strain rate) is proposed to quantify particle breakage during shear. The breakage effect on the elastic stiffness is not verified, and the formulation follows constitutive equations proposed by Einav [22]. Owing to the irreversible nature of particle breakage, the breakage acts as an elastic–plastic coupling variable. Comparisons between the proposed model predictions and experimental data indicate reasonable performance of the model. For the sake of comparison, predictions obtained from the hypoplastic model of Engin et al. [25] specially developed for simulation of crushable sands are also included.

2 Fundamentals of constitutive equations for crushable sands

A definition of an index quantifying the extent of particle breakage is crucial in the mechanics of crushable media. Various types of relative breakage indexes have been proposed to quantify breakage in crushable granular soils in terms of the breakage-induced evolution of the GSD curve [59, 65, 67]. Einav [22] introduced a breakage index (i.e., B) varying from zero at initial state (i.e., nil breakage) to 1 at the ultimate grading which the crushable soil finally will approach. B is mathematically defined as the ratio of the area between the current and initial GSDs (i.e., B_t) to the area between the ultimate and initial GSDs (i.e., B_p) [see Fig. 1]:

$$B = \frac{B_t}{B_p} = \frac{\int_{D_m}^{D_M} [F(D) - F_0(D)]d(\log(D))}{\int_{D_m}^{D_M} [F_u(D) - F_0(D)]d(\log(D))} \quad (1)$$

in Eq. (1), D stands for the grain size. D_m and D_M indicate, respectively, the minimum and maximum particle sizes, and $F_0(D)$, $F(D)$, and $F_u(D)$ represent the initial, current, and

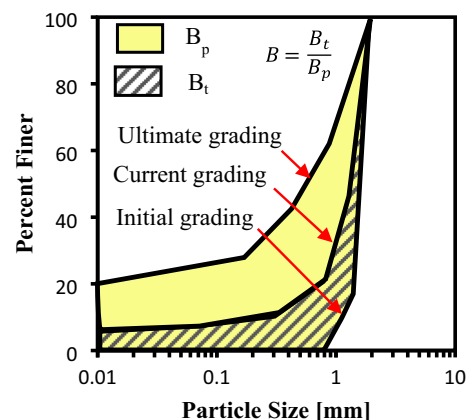


Fig. 1 Definition of the particle breakage index of Einav [22]

and ultimate GSDs, respectively. Evolution of particle breakage would terminate asymptotically once a GSD approaches its ultimate fractal distribution e.g., [22]. For this reason, $F(D)$ evolves from $F_0(D)$ to $F_u(D)$ through [22]:

$$F(D) = F_0(D)(1 - B) + F_u(D)B \tag{2}$$

in Eq. (2), $F_0(D) = (D/D_M)^{\beta_1}$ and $F_u(D) = (D/D_M)^{\beta_2}$ wherein β_1 and β_2 are soil constants.

Stiffness and mobilization of shear strength in sand-fine mixtures depend on fines content, and contribution of the coarse and fine fractions in the load transfer mechanism is a function of coarse to fine size ratio e.g., [17, 61, 66, 75, 88, 102]. Applying the discrete element method (DEM), Einav [22] suggested that the energy stored in soil grains depends on their size, and thus, larger particles have greater stored energy compared to the fines. When a crushable granular soil is subjected to shear, the breakage-induced fines surround larger particles, but do not participate in the load-bearing microstructure actively [22, 127], consequently, they (i.e., fines) do not store energy [22]. Therefore, the elastic energy functions in addition to the effective stress or strain invariants should also incorporate some measures of GSD. According to the breakage mechanics theory of Einav [23], the Helmholtz free energy function can be expressed in terms of the elastic strains and breakage index by applying the gradation curve as the average weighted function on microscopic variables, through a statistical homogenization process as:

$$H = H_1(\varepsilon_v^e, \varepsilon_q^e)(1 - \nu B) \tag{3}$$

where ε_v^e and ε_q^e are elastic volumetric and shear strains, respectively. $H_1(\varepsilon_v^e, \varepsilon_q^e)$ is the Helmholtz free energy function for nil particle breakage, and ν , a proximity index indicating the distance between the ultimate and the initial GSDs, is determined as:

$$\nu = 1 - \frac{\langle D \rangle_0^2}{\langle D \rangle_u^2} \tag{4}$$

where in $\langle D \rangle_0^2$ and $\langle D \rangle_u^2$ are, respectively, the second-order moments of the initial and ultimate GSDs.

The effective stress variables in triaxial space can be calculated from the modified Helmholtz free energy function as:

$$p' = \frac{\partial H}{\partial \varepsilon_v^e}; \quad q = \frac{\partial H}{\partial \varepsilon_q^e} \tag{5}$$

wherein $p' = (\sigma'_a + 2\sigma'_r)/3$ and $q = \sigma'_a - \sigma'_r$ are, respectively, the mean principal effective stress and shear stress (of note, σ'_a and σ'_r are the axial and radial principal stresses acting on a triaxial specimen). Further differentiation of Eq. (5) yields the rates of the effective stress invariants:

$$\begin{aligned} \dot{p}' &= \frac{\partial^2 H}{\partial \varepsilon_v^e \partial \varepsilon_v^e} \dot{\varepsilon}_v^e + \frac{\partial^2 H}{\partial \varepsilon_v^e \partial \varepsilon_q^e} \dot{\varepsilon}_q^e + \frac{\partial^2 H}{\partial \varepsilon_v^e \partial B} \dot{B} \\ &= H_{,\nu\nu} \dot{\varepsilon}_v^e + H_{,\nu q} \dot{\varepsilon}_q^e + H_{,\nu B} \dot{B} \\ \dot{q} &= \frac{\partial^2 H}{\partial \varepsilon_q^e \partial \varepsilon_v^e} \dot{\varepsilon}_v^e + \frac{\partial^2 H}{\partial \varepsilon_q^e \partial \varepsilon_q^e} \dot{\varepsilon}_q^e + \frac{\partial^2 H}{\partial \varepsilon_q^e \partial B} \dot{B} \\ &= H_{,qv} \dot{\varepsilon}_v^e + H_{,qq} \dot{\varepsilon}_q^e + H_{,qB} \dot{B} \end{aligned} \tag{6}$$

For the sake of brevity, $\partial^2 H / \partial \varepsilon_v^e \partial \varepsilon_v^e = H_{,\nu\nu}$, $\partial^2 H / \partial \varepsilon_q^e \partial \varepsilon_q^e = H_{,qq}$, $\partial^2 H / \partial \varepsilon_v^e \partial \varepsilon_q^e = \partial^2 H / \partial \varepsilon_q^e \partial \varepsilon_v^e = H_{,\nu q} = H_{,qv}$, $\partial^2 H / \partial \varepsilon_v^e \partial B = H_{,\nu B}$, and $\partial^2 H / \partial \varepsilon_q^e \partial B = H_{,qB}$. Rearrangement of terms in Eq. (6) renders the following relations for the elastic strain rates:

$$\begin{aligned} \left\{ \begin{matrix} \dot{\varepsilon}_v^e \\ \dot{\varepsilon}_q^e \end{matrix} \right\} &= \frac{1}{\det \Theta} \underbrace{\begin{bmatrix} H_{,qq} & -H_{,\nu q} \\ -H_{,qv} & H_{,\nu\nu} \end{bmatrix}}_{(I)} \left\{ \begin{matrix} \dot{p}' \\ \dot{q} \end{matrix} \right\} \\ &\quad - \underbrace{\frac{\dot{B}}{\det \Theta} \begin{bmatrix} H_{,qq} & -H_{,\nu q} \\ -H_{,qv} & H_{,\nu\nu} \end{bmatrix}}_{(II)} \left\{ \begin{matrix} H_{,\nu B} \\ H_{,qB} \end{matrix} \right\} \end{aligned} \tag{7}$$

wherein the 2×2 Hessian matrix is calculated from $\Theta = \begin{bmatrix} H_{,\nu\nu} & H_{,\nu q} \\ H_{,qv} & H_{,qq} \end{bmatrix}$. Recalling that the Helmholtz free energy in Eq. (3) depends on ε_v^e , ε_q^e and B , Eq. (7) necessitates that the total elastic strain rates become functions of $\dot{\varepsilon}_v^e$, $\dot{\varepsilon}_q^e$ and \dot{B} . The particle breakage is an irreversible phenomenon [see Guo and Zhu [33] for discussion] which itself is capable of affecting the elastic response of crushable sands through the participation of \dot{B} , $H_{,\nu B}$ and $H_{,qB}$ in Eq. (7). Therefore, the total elastic volumetric and shear strain rates in Eq. (7) are decomposed into two terms with completely different physical interpretations: (i) the term (I) which is reversible upon effective stress reversal, and (ii) the breakage-dependent term (II) which is irreversible. Accordingly, the total elastic strain rates are irreversible with effective stress rates unless under nil particle breakage (say $\dot{B} = 0$) which occurs on the condition that sand behaves purely elastic. For this reason, B as an irreversible variable can be interconnected to a proper hardening variable to bear the role of an elastic–plastic coupling factor. In this sense, B increases progressively with plastic strains in the elastic–plastic regime of the behavior and remains unchanged ($\dot{B} = 0$) given that soil behaves purely elastic. In the modern continuum mechanics, free energy functions incorporate a supplemental internal variable depending on the hardening parameter(s) to account for the effect of elastic–plastic coupling e.g., [13, 40, 41]. Of note, the coupling between elasticity and plasticity has been addressed in the pertinent

literature of geomechanics e.g., [13, 28, 29, 31, 40, 41, 64]. Using the concept of alternative decomposition of strains for coupled materials by Collins and Houlsby [13], the total volumetric and shear strain rates can be expressed as the elastic reversible and irreversible rates:

$$\begin{aligned} \dot{\epsilon}_v &= \dot{\epsilon}_v^e + \dot{\epsilon}_v^p = \underbrace{\dot{\epsilon}_v^{er} + \dot{\epsilon}_v^{ei}}_{\dot{\epsilon}_v^e} + \dot{\epsilon}_v^p = \dot{\epsilon}_v^{er} + \underbrace{\dot{\epsilon}_v^{ei} + \dot{\epsilon}_v^p}_{\dot{\epsilon}_v^i} = \dot{\epsilon}_v^{er} + \dot{\epsilon}_v^i \\ \dot{\epsilon}_q &= \dot{\epsilon}_q^e + \dot{\epsilon}_q^p = \underbrace{\dot{\epsilon}_q^{er} + \dot{\epsilon}_q^{ei}}_{\dot{\epsilon}_q^e} + \dot{\epsilon}_q^p = \dot{\epsilon}_q^{er} + \underbrace{\dot{\epsilon}_q^{ei} + \dot{\epsilon}_q^p}_{\dot{\epsilon}_q^i} \end{aligned} \tag{8}$$

In Eq. (8), $\dot{\epsilon}_x^{er}$, $\dot{\epsilon}_x^{ei}$ and $\dot{\epsilon}_x^i$ with $x \in \{v, q\}$ are, respectively, the elastic reversible, elastic irreversible, and total irreversible strain rates. Using Eqs. (7) and (8), one has:

$$\begin{aligned} \begin{Bmatrix} \dot{\epsilon}_v^{ei} \\ \dot{\epsilon}_q^{ei} \end{Bmatrix} &= \frac{1}{\det \Theta} \begin{bmatrix} H_{,qq} & -H_{,vq} \\ -H_{,qv} & H_{,vv} \end{bmatrix} \begin{Bmatrix} \dot{p}' \\ \dot{q} \end{Bmatrix} \\ \begin{Bmatrix} \dot{\epsilon}_v^i \\ \dot{\epsilon}_q^i \end{Bmatrix} &= \underbrace{\frac{-B}{\det \Theta} \begin{bmatrix} H_{,qq} & -H_{,vq} \\ -H_{,qv} & H_{,vv} \end{bmatrix} \begin{Bmatrix} H_{,vB} \\ H_{,qB} \end{Bmatrix}}_{\begin{Bmatrix} \dot{\epsilon}_v^{ei} & \dot{\epsilon}_q^{ei} \end{Bmatrix}^T} + \begin{Bmatrix} \dot{\epsilon}_v^p \\ \dot{\epsilon}_q^p \end{Bmatrix} \end{aligned} \tag{9}$$

Rearranging the terms in the first part of Eq. (9) yields:

$$\begin{Bmatrix} \dot{p}' \\ \dot{q} \end{Bmatrix} = \Theta \begin{Bmatrix} \dot{\epsilon}_v^{er} \\ \dot{\epsilon}_q^{er} \end{Bmatrix} = \begin{bmatrix} H_{,vv} & H_{,vq} \\ H_{,qv} & H_{,qq} \end{bmatrix} \begin{Bmatrix} \dot{\epsilon}_v^{er} \\ \dot{\epsilon}_q^{er} \end{Bmatrix} \tag{10}$$

Equation (10) resembles the theory of Graham and Houlsby [32] for anisotropic soils in the triaxial space:

$$\begin{Bmatrix} \dot{p}' \\ \dot{q} \end{Bmatrix} = \underbrace{\begin{bmatrix} K & J \\ J & 3G \end{bmatrix}}_{\Theta} \begin{Bmatrix} \dot{\epsilon}_v^{er} \\ \dot{\epsilon}_q^{er} \end{Bmatrix} \tag{11}$$

where G, K and J are the elastic shear, bulk and shear-volumetric moduli, respectively. J denotes the stress-induced anisotropy impact on the elastic behavior e.g., [5, 23, 31, 37, 38]. The consideration of the influence of anisotropy in the elastic domain plays a significant role in predicting shear strength of sands subjected to undrained cyclic loading e.g., [28, 29, 60, 82] as well as of fine-grained soils e.g., [95, 96, 97, 98, 99, 111]. Now, comparing Eqs. (10) and (11) results in the following elastic moduli:

$$H(\epsilon_v^e, \epsilon_q^e, B) = H_1(\epsilon_v^e, \epsilon_q^e)(1 - \nu B) = \underbrace{p_{ref} V^{\frac{\chi}{1-\chi}} \left[\frac{1}{(2-\chi)\bar{K}} V^2 + \frac{3}{2} \bar{G} \epsilon_q^e \right]}_{H_1(\epsilon_v^e, \epsilon_q^e)} (1 - \nu B) \tag{13}$$

with

$$V = \left(\frac{p'_0}{p_{ref}} \right)^{1-\chi} + (1-\chi)\bar{K}\epsilon_v^e$$

$$K = H_{,vv}; G = \frac{1}{3}H_{,qq}; J = H_{,vq} = H_{,qv} \tag{12}$$

Using resonance column tests, Iwasaki and Tatsuoka [51] reported that at a fixed void ratio, the shear modulus is influenced by variations in the GSD curve. Wichtmann and Triantafyllidis [110] revealed that G decreases with increasing uniformity coefficient in granular soils. Given that the GSD varies with respect to the progression of particle breakage [3, 35, 59, 65] then particle breakage can affect the elastic moduli of soils. As the Helmholtz free energy is a function of particle breakage according to Eq. (3), also the elastic moduli will be influenced by the change in GSD.

The hyper-elastic part has been conjugated to an elasto-plastic theory which is the Simple Anisotropic Sand Model (SANISAND) proposed by Dafalias and Manzari [16]. Many studies extended the SANISAND version proposed by Dafalias and Manzari [16] by adding a second yield criteria e.g., [101], by taking into account the anisotropic behavior of soils e.g., [60], by omitting the elastic range of the behavior e.g., [63], or by adding a memory surface [70]. But, the original version is not only simple but also robust enough to predict the behavior of granular materials over a wide range of initial confining pressures and dry densities. Besides this, the 2004 version is still most widely used in geotechnical practice and also in the calculation of boundary value problems in research [56, 71].

3 A hyperelastic-plastic model accounting for particle breakage and elastic–plastic coupling

Jiang and Liu [52] suggested two Helmholtz free energy functions for nonlinear hyperelastic response of soils dependent on $p'^{1/3}$ (i.e., Hertz-type elasticity) and $p'^{1/2}$ (i.e., Goddard-type elasticity). Ashkar and Lashkari [2] suggested an extended Jiang and Liu [52] Helmholtz free energy function to obtain hyperelastic response dependent on p'^{χ} with $\chi \in [0, 1)$. A revised form of the latter Helmholtz free energy function with the purpose of incorporating the particle breakage is adopted here (see Eq. 13):

wherein p'_0 is confining pressure at nil elastic strain and $p_{ref} = 100$ [kPa] is a reference normalizing stress. B in Eq. (13) remains unchanged when the soil behaves purely elastic. However, B evolves progressively in the elastic–plastic regime of the behavior to reach its asymptotic value at the critical state. Equation (12) in combination with Eq. (13) results in the following pressure-dependent hyperelastic moduli:

$$\begin{aligned}
 K &= \bar{K} p_{ref} (1 - \nu B)^{1-\chi} \left(\frac{p'}{p_{ref}} \right)^\chi \theta^\chi \left[1 + \frac{\chi(2\chi - 1)}{6} \cdot \frac{\bar{K}}{\bar{G}} \cdot \left(\frac{\eta}{\theta} \right)^2 \right] \\
 G &= \bar{G} p_{ref} (1 - \nu B)^{1-\chi} \left(\frac{p'}{p_{ref}} \right)^\chi \theta^\chi \\
 J &= \chi \bar{K} p_{ref} \left(\frac{\eta}{\theta} \right) (1 - \nu B)^{1-\chi} \left(\frac{p'}{p_{ref}} \right)^\chi \theta^\chi
 \end{aligned}
 \tag{14}$$

where $\eta = q/p'$ is stress ratio, and $\bar{G} = G_0 F(e)$ and $\bar{K} = K_0 F(e)$ are non-dimensional parameters dependent on the void ratio e with $F(e) = (2.97 - e)^2 / (1 + e)$ proposed by Hardin and Richart [36]. G_0 and K_0 are material parameters. In Eq. (14), θ is defined as:

$$\theta = \frac{1}{2} \left(1 + \sqrt{1 - \frac{2\chi}{3} \left(\frac{\bar{K}}{\bar{G}} \right) \eta^2} \right)
 \tag{15}$$

Hence, Eq. (14) describes the hyperelastic moduli as pycnotropy (i.e., void ratio-dependent) as well as barotropy (i.e., pressure-dependent) functions. Of note, Eq. (14) signifies that Eq. (13) is capable of reproducing p'^χ -dependent hyperelastic moduli through the entire range of $\chi \in [0, 1]$; however, the basic Helmholtz free energy functions of Jiang and Liu [52] are only compelling for $\chi = 1/3$ and $1/2$. Moreover, the evolving GSD as an elastic–plastic coupling phenomenon is captured through the explicit participation of B in the hyperelastic and Helmholtz breakage coupling moduli [see the second part of Eq. (9)]:

$$H_{,\nu B} = -\nu p_{ref} V^{\frac{1}{1-\chi}} \left[1 + \frac{3}{2} \frac{\bar{K}}{\bar{G}} \chi \left(\frac{\varepsilon_q^e}{V} \right)^2 \right]
 \tag{16}$$

$$H_{,qB} = -3\nu p_{ref} \bar{G} \varepsilon_q^e V^{\frac{\chi}{1-\chi}}$$

Appendix 1 illustrates the evaluation of the hyperelastic formulation of the proposed model.

3.1 Yield function

A narrow open wedge-type yield function is adopted from Dafalias and Manzari [16]:

$$f(\eta, \alpha) = |\eta - \alpha| - m = 0
 \tag{17}$$

wherein m defines opening of the yield function (per default: $m = 0.001$). Back-stress ratio, i.e., α , is a kinematic hardening variable indicating rotation of the bisector of the yield function with respect to the e vs. p' -axis see [16]. Soil behaves purely

elastic (i.e., elastic strains become completely reversible) as long as the effective stress state is located inside the yield function [say $f(\eta, \alpha) < 0$], whereas plastic strains are generated once the effective stress state reaches the yield function [i.e., $f(\eta, \alpha) = 0$] and attempts to change the back-stress ratio (say kinematic hardening variable).

3.2 CSL and state parameter

To investigate the critical state properties of crushable granular soils, results of a series of drained triaxial tests on Tacheng rockfill from [118, 120] are discussed here. The tests were conducted at four initial void ratios (i.e., 0.189, 0.244, 0.285, and 0.317), and three initial confining pressures (i.e., 0.4, 0.8, and 1.6 MPa). Figure 2a demonstrates the CSLs of Tacheng rockfill in the e vs. $(p'/p_{ref})^\xi$ plane with $\xi = 0.7$. The CSL incorporating the effect of grain crushing in the e - p' - B space becomes [39]:

$$e_{cs} = e_\Gamma - \lambda \left(\frac{p'}{p_{ref}} \right)^\xi
 \tag{18}$$

with

$$e_\Gamma = e_i + (e_u - e_i) \frac{B}{a + B}$$

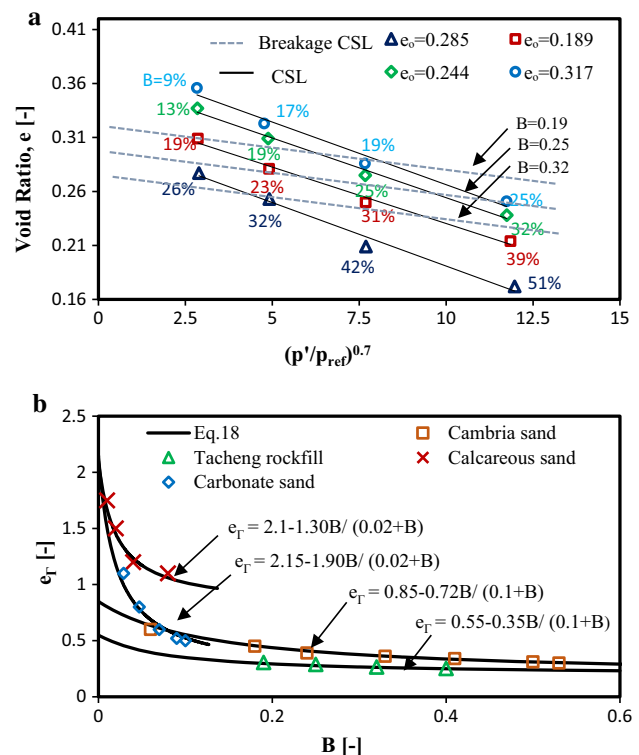


Fig. 2 Effect of particle breakage on the critical state void ratio: **a** conventional and breakage CSLs in the e vs. $(p'/p_{ref})^\xi$ plane and **b** change in e_Γ following increase in B (data from 117, 119, Yamamuro and Lade [123], Wei et al. [112], and Wang et al. [109])

whereby ξ is a model constant, and λ is the slope of the CSL in the e vs. $(p'/p_{ref})^\xi$ plane. “a” is a model parameter controlling the pace of relocation of CSL in the e vs. $(p'/p_{ref})^\xi$ plane with particle breakage. e_i and e_u are, respectively, soil parameters related to the initial (corresponding to $B = 0$) and ultimate (as $B \rightarrow 1$) positions of the CSL in the e vs. $(p'/p_{ref})^\xi$ plane. Increase in fines owing to breakage of coarser parent particles in crushable granular soils causes gradual changes in the intercept (i.e., e_Γ) and slope (i.e., λ) of the CSL in the e vs. $(p'/p_{ref})^\xi$ plane e.g., [3, 127]. However, change in λ is practically negligible in comparison with the change in e_Γ e.g., [10, 30, 62, 78]. Breakage CSLs can be established considering critical states with the same breakage indices, as illustrated in Fig. 2a and are used herein solely for the determination of e_i and e_u . Recently, Lashkari et al. [62] suggested that change in λ becomes noticeable only once the fines fraction becomes so large that the mechanical behavior of the mixture transfers from the “fines-in-coarse” regime to the “coarse-in-fine” one. In Fig. 2b, the predicted e_Γ vs. B curves using Eq. (18) agree reasonably with the corresponding laboratory data of [117, 119] on Tacheng rockfill, Yamamuro and Lade [123] on Cambria sand, Wei et al. [112] on calcareous sand, and Wang et al. [109] on carbonate sand.

Now, the modified state parameter of Been and Jefferies [4] which is the Euclidean distance between the current soil state from the breakage-dependent CSL in the e vs. p' plane can be incorporated into the constitutive model:

$$\psi = e - e_{cs} \tag{19}$$

wherein e is the current void ratio and e_{cs} is the critical state void ratio calculated from Eq. (18) corresponding to the current values of p' and B .

3.3 Plastic strain rates

A stress ratio-driven mechanism in triaxial space suggested by Dafalias and Manzari [16] is employed here for the calculation of the plastic shear strain rate:

$$\dot{\epsilon}_q^p = \frac{\dot{\eta}}{K_p} = s \langle L \rangle \tag{20}$$

whereby L is the loading index representing the magnitude of the plastic shear strain rate. The Macaulay brackets $\langle L \rangle$ denote $\langle L \rangle = L$ in case of $L > 0$, and $\langle L \rangle = 0$ if $L \leq 0$. In Eq. (20), s is determined according to the location of the stress ratio with respect to α as the bisector of the yield function, $s=1$ if $\eta - \alpha = m$ and $s = -1$ when $\alpha - \eta = m$. The plastic hardening modulus K_p is defined by e.g., [31, 64]:

$$K_p = h(1 - c_h e) \frac{\alpha_b - \alpha}{|\alpha - \alpha_{in}|} \left(\frac{p'}{p_{ref}} \right)^{\lambda - 1} \tag{21}$$

wherein h and c_h are model constants. α_{in} is the initial value of α at the beginning of the most recent shear loading.

The dilatancy, d , defined as the ratio between the rate of irreversible volumetric strain and the rate of irreversible shear strain is expressed as e.g., [31, 64]:

$$d = \frac{\dot{\epsilon}_v^i}{s \dot{\epsilon}_q^i} = \frac{\dot{\epsilon}_v^{ei} + \dot{\epsilon}_v^p}{s(\dot{\epsilon}_q^{ei} + \dot{\epsilon}_q^p)} = d_0(\alpha_d - s\alpha) \tag{22}$$

wherein d_0 is a material constant, and α_d is dilatancy back-stress ratio. Similar to Dafalias and Manzari [16], α_b [see Eq. (21)] and α_d [see Eq. (22)] are calculated from:

$$\begin{aligned} \alpha_b &= M_b - m = \overbrace{M \exp(-n_b \psi)}^{M_b} - m \\ \alpha_d &= M_d - m = \overbrace{M \exp(+n_d \psi)}^{M_d} - m \end{aligned} \tag{23}$$

In Eqs. (23), M is the slope of the CSL in the q - p' plane. M_d and M_b are dilatancy and peak stress ratios, respectively. n_d and n_b are model constants, determining the impact of the state parameter on the dilatancy and peak stress ratios, respectively.

Now, using Eqs. (12), 9(b), (20), and (22), the volumetric plastic strain rate is calculated from:

$$\dot{\epsilon}_v^p = \langle L \rangle d + \left[\frac{(3G + sJd)H_{,vB} - (J + sKd)H_{,qB}}{3GK - J^2} \right] \dot{B} \tag{24}$$

3.4 Rates of the effective stress invariants and loading index

The rates of the effective stress invariants are calculated using Eqs. (6), (8), and (12) as:

$$\begin{aligned} \dot{p}' &= K \dot{\epsilon}_v + J \dot{\epsilon}_q - K \dot{\epsilon}_v^p - J \dot{\epsilon}_q^p + H_{,vB} \dot{B} \\ \dot{q} &= J \dot{\epsilon}_v + 3G \dot{\epsilon}_q - J \dot{\epsilon}_v^p - 3G \dot{\epsilon}_q^p + H_{,qB} \dot{B} \end{aligned} \tag{25}$$

Recalling that $\dot{\eta} = [\dot{q} - \eta \dot{p}'] / p'$, substitution of Eqs. (24) and (25) in $\dot{\eta} = s K_p \langle L \rangle$ [see Eq. (20)] renders the following relation for the loading index:

$$L = \frac{(3G - \eta J) \dot{\epsilon}_q + (J - \eta K) \dot{\epsilon}_v + (C_1 H_{,qB} + C_2 H_{,vB}) \dot{B}}{s(p' K_p + 3G - \eta J + s[J - \eta K]d)} \geq 0$$

with

$$C_1 = 1 - \frac{(K\eta - J)(J + sKd)}{3GK - J^2}$$

and

$$C_2 = \frac{(K\eta - J)(3G + sJd)}{3GK - J^2} - \eta$$

$$\tag{26}$$

Table 1 B , W^p , and W^p_q of Tacheng rockfill specimens at the end of drained triaxial tests (experiments performed by [117, 119])

p'_o [MPa]	e_o [-]	B [-]	W^p [MPa]	W^p_q [MPa]
0.4	0.189	0.322	0.209	0.262
0.8	0.189	0.424	0.447	0.478
1.6	0.189	0.516	0.906	0.856
0.4	0.317	0.161	0.238	0.243
0.8	0.317	0.192	0.517	0.474
1.6	0.317	0.253	0.983	0.813

3.5 Breakage index

Magnitude and spatial distribution of particle level contact forces in consequence of imposed stress path and strain level are key controlling factors for an individual particle to crush e.g., [20]. It is believed that the element level

plastic work can be implemented as an appropriate factor taking into account the combined influence of the effective stress path and plastic strain magnitude e.g., [53, 69, 84]. Void ratio also governs the stress–strain–strength response of the granular soils and affects the evolution of microstructure and breakage of particles under both drained and undrained conditions. Particles in loose assemblies have greater space for sliding, rolling, and soil skeleton adjustment than dense assemblies at the same effective stress level. This phenomenon results in larger volumetric strains, thus dissipating greater plastic work in loose granular soils. Table 1 shows the breakage index B , plastic work (i.e., W^p) and plastic shear work (i.e., W^p_q) for loose and dense Tacheng rockfill specimens under drained condition. According to Table 1, B for dense specimens ($e_o = 0.189$) is greater than that of the loose specimens ($e_o = 0.317$) at the same initial confining pressure. On the other hand, W^p for the dense specimen is less than that of the loose ones. Hence, the use of W^p would overestimate B of

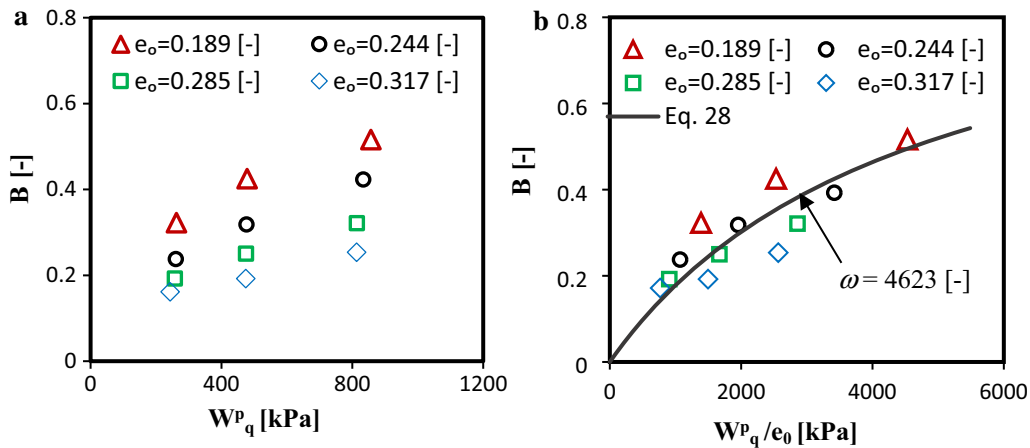


Fig. 3 Variation of breakage index for Tacheng rockfill with: **a** W^p_q and **b** W^p_q/e_o (data from [117, 119])

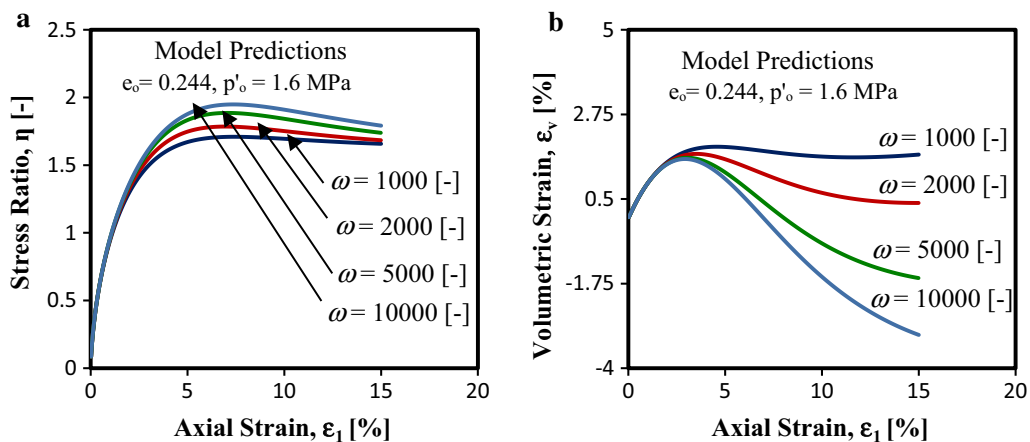


Fig. 4 Influence of ω on the constitutive model prediction of a drained triaxial test on a Tacheng rockfill specimen: **a** mobilization of stress ratio and **b** volume change response

Table 2 The proposed model parameters used for simulation of Toyoura, Cambria, Kurnell, and Aio sands as well as Tacheng rockfill behavior

Sand name	Elasticity	CSL	Dilatancy	Plastic hardening	Breakage
Toyoura	$G_0=50$ $K_0=0.75 G_0$ $\chi=0.95$	$M_c=1.25$ $M_e=0.7M_c$ $\lambda=1.9 \times 10^{-2}$ $e_i=e_u=0.93$ $\xi=0.70$	$d_0=0.95$ $n_d=2.50$	$c_h=0.97$ $h=224.90$ $n_b=1$	–
Tacheng rockfill	$G_0=125$ $K_0=0.75 G_0$ $\chi=0.95$	$M_c=1.68$ $\lambda=3 \times 10^{-3}$ $e_i=0.55$ $e_u=0.19$ $\xi=0.7$	$d_0=1.5$ $n_d=0.3$	$c_h=0.97$ $h=70.1$ $n_b=1.5$	$\nu=0.9$ $\omega=4623$ $a=0.1$ $\beta_1=1.1$ $\beta_2=0.3$
Cambria	$G_0=125$ $K_0=0.75 G_0$ $\chi=0.95$	$M_c=1.43$ $\lambda=4.5 \times 10^{-3}$ $e_i=0.85$ $e_u=0.13$ $\xi=0.7$	$d_0=1.3$ $n_d=1.5$	$c_h=0.97$ $h=35.1$ $n_b=1.0$	$\nu=0.70$ $\omega=19,230$ $a=0.10$ $\beta_1=5.2$ $\beta_2=0.4$
Kurnell	$G_0=45$ $K_0=0.75 G_0$ $\chi=0.95$	$M_c=1.45$ $\lambda=1.2 \times 10^{-2}$ $e_i=0.97$ $e_u=0.77$ $\xi=0.7$	$d_0=0.9$ $n_d=2.2$	$c_h=0.97$ $h=75.1$ $n_b=1.3$	$\nu=0.5$ $\omega=5498$ $a=0.04$ $\beta_1=1.7$ $\beta_2=0.4$
Aio	$G_0=50$ $K_0=0.75 G_0$ $\chi=0.85$	$M_c=1.60$ $M_e=0.65 M_c$ $\lambda=11 \times 10^{-2}$ $e_i=1.8$ $e_u=0.8$ $\xi=0.3$	$d_0=0.35$ $n_d=0.6$	$c_h=0.87$ $h=110.9$ $n_b=1.1$	$\nu=0.6$ $\omega=12,770$ $a=0.01$ $\beta_1=1.2$ $\beta_2=0.76$

the loose specimens compared to the dense ones. On contrary, W_q^p data are consistent with the trending of B. Therefore, we propose to interrelate B to W_q^p , which reads:

$$\dot{W}_q^p = q \dot{\varepsilon}_q^p \quad (27)$$

Figure 3 illustrates the variations of B with W_q^p and e_0 for Tacheng rockfill. A hyperbolic relationship between B and W_q^p normalized by the initial void ratio, i.e., W_q^p/e_0 , in the following form can fit reasonably the laboratory data:

$$B = 1 - \frac{\omega}{\omega + W_q^p/e_0} \quad (28)$$

wherein ω is a dimensionless model constant and changes pace of B with W_q^p/e_0 . To demonstrate the function of ω , the predicted η vs. ε_1 and ε_v vs. ε_1 curves for $\omega = 1000, 2000, 5000, \text{ and } 10,000$ [–] obtained from the constitutive model for a Tacheng rockfill specimen with $e_0 = 0.244$ sheared under drained condition from $p'_0 = 1.6$ [kPa] are plotted in Fig. 4. At a fixed axial strain, B increases with decrease in ω . Accordingly, the peak stress ratio vanishes and the volume change response tends to contract with

increase in B. Since B associated with elevated pressures is beyond the scope of this research, W_q^p , rather than W^p , was adopted here to circumvent overestimation of the shear-induced breakage in loose sands. Implementation of a narrow but closed yield function [instead of the wedge-type yield function of Eq. (17)] together with a second plastic hardening mechanism that is activated under loading with limited or even nil change in η can further improve the constitutive model predictive capacity. Under the latter circumstance, ε_v^p or work due to the plastic volumetric strain must be hired for the second yield mechanism accounting for particle breakage occurring under isotropic or K_0 compression. Using Eq. (28), rate of the breakage index (i.e., \dot{B}) becomes:

$$\dot{B} = \frac{1}{\omega e_0} (1 - B)^2 \dot{W}_q^p \quad (29)$$

Equation (29) signifies that B remains unchanged as long as soil behaves purely elastic (of note, $\dot{W}_q^p = 0$ when soil behaves purely elastic) and increases progressively with W_q^p until the ultimate GSD is attained at $B = 1$.

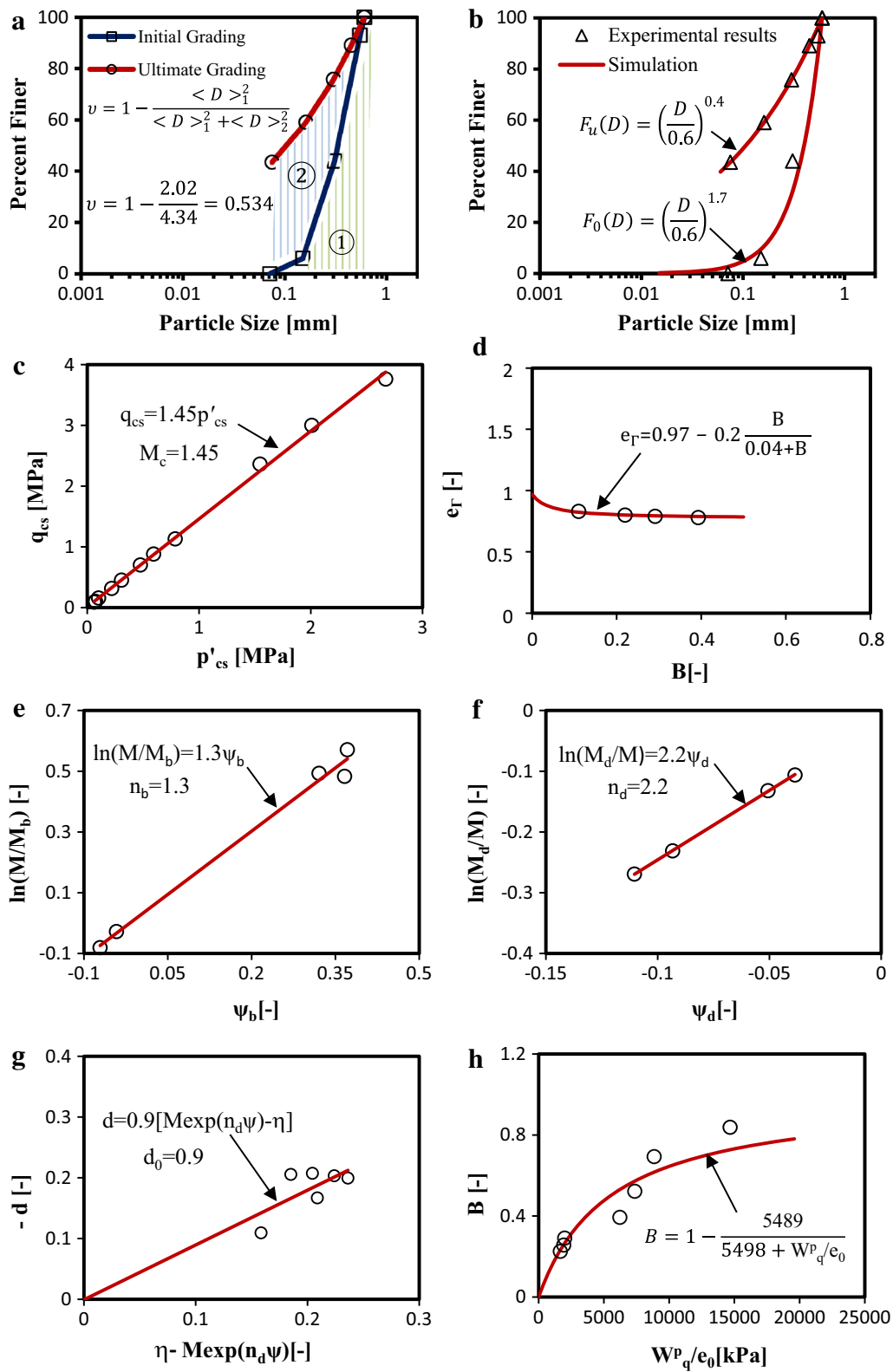


Fig. 5 The model constants for Kurnell sand (experiments performed by Russell and Khalili [91])

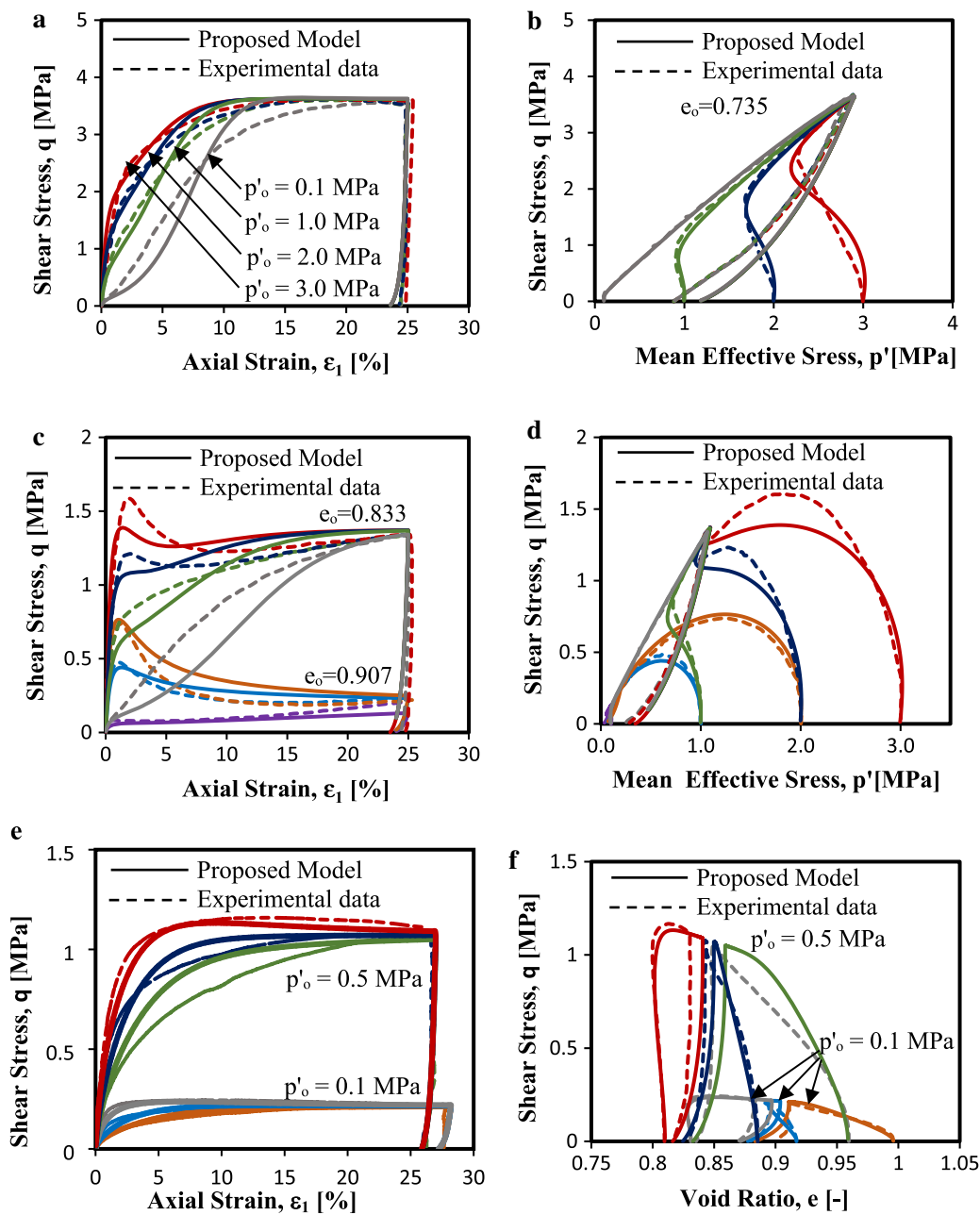


Fig. 6 The proposed constitutive model predictions versus experimental data of Toyoura sand for: **a** and **b** four undrained tests on medium-dense specimens ($e_0 = 0.735$); **c** and **d** seven undrained tests on medium-loose ($e_0 = 0.833$) and loose ($e_0 = 0.907$) specimens; **e** and **f** six drained tests on loose to very loose specimens (data from Verdugo and Ishihara [106])

4 Calibration of the model

The proposed model parameters can be classified into five different categories: (i) parameters related to the elastic response, (ii) CSL parameters, (iii) dilatancy parameters, (iv) plastic hardening modulus parameters, and (v) parameters related to breakage of particles (see Table 2).

G_0 can be determined from experimental data of bender element and resonant column tests or by using the initial

slope of the q vs. ε_q curves, where small strains prevail. \bar{G} and χ can be found using the data of the elastic shear modulus in the small strain levels such as results of bender element and resonant column tests. At extremely low shear strain levels, Eq. (14) yields:

$$G = \bar{G} p_{ref} \left(\frac{p'}{p_{ref}} \right)^\chi \tag{30}$$

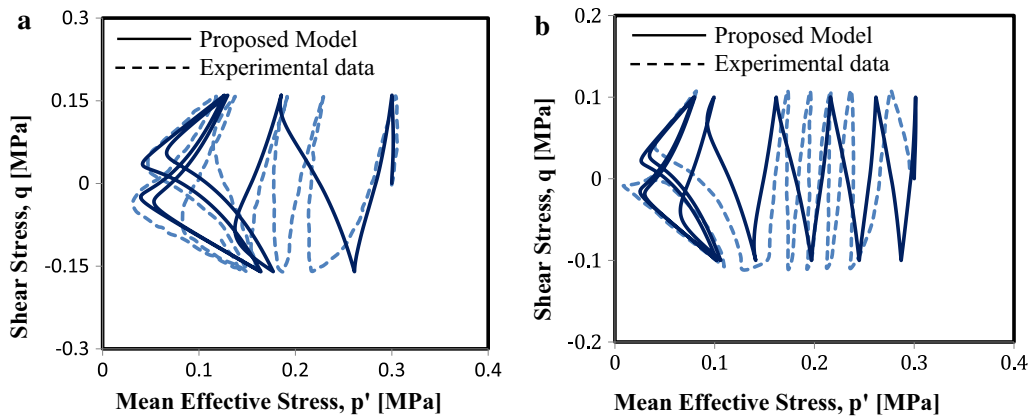


Fig. 7 The proposed constitutive model predictions versus experimental data of two undrained cyclic tests on Toyoura sand specimens sheared from $p'_0 = 0.3$ [MPa]: **a** $e_0 = 0.79$ [data from Yang and Sze [124]] and **b** $e_0 = 0.80$ (data from Ishihara and Towhata [50])

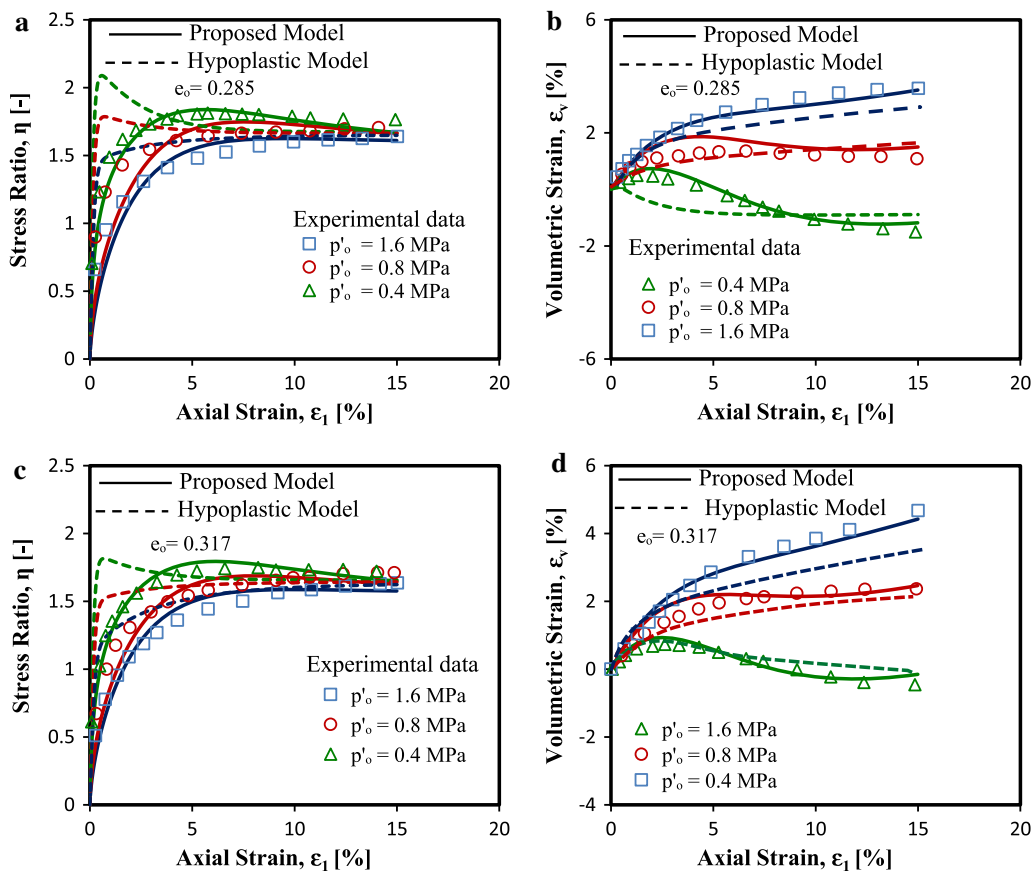


Fig. 8 The proposed and hypoplastic models predictions for mobilization of stress ratio and volume change behavior of six Tacheng rockfill specimens sheared under drained condition from $p'_0 = 0.4, 0.8$ and 1.6 [MPa]: **a** and **b** three specimens with $e_0 = 0.285$; **c** and **d** three specimens with $e_0 = 0.317$ (data from [117, 119])

By taking logarithm from both sides of Eq. (30), it can be re-written as:

$$\ln G = \ln(\bar{G} p_{ref}) + \chi \ln\left(\frac{p'}{p_{ref}}\right) \quad (31)$$

Hence $\ln(\bar{G} p_{ref})$ and χ can be determined, respectively, as the intercept and slope of the best straight line fitted to the experimental data in the $\ln G$ vs. $\ln(p'/p_{ref})$ plane. $K_0 \approx (0.7 \text{ to } 0.9) G_0$ is a reasonable assumption for various sands.

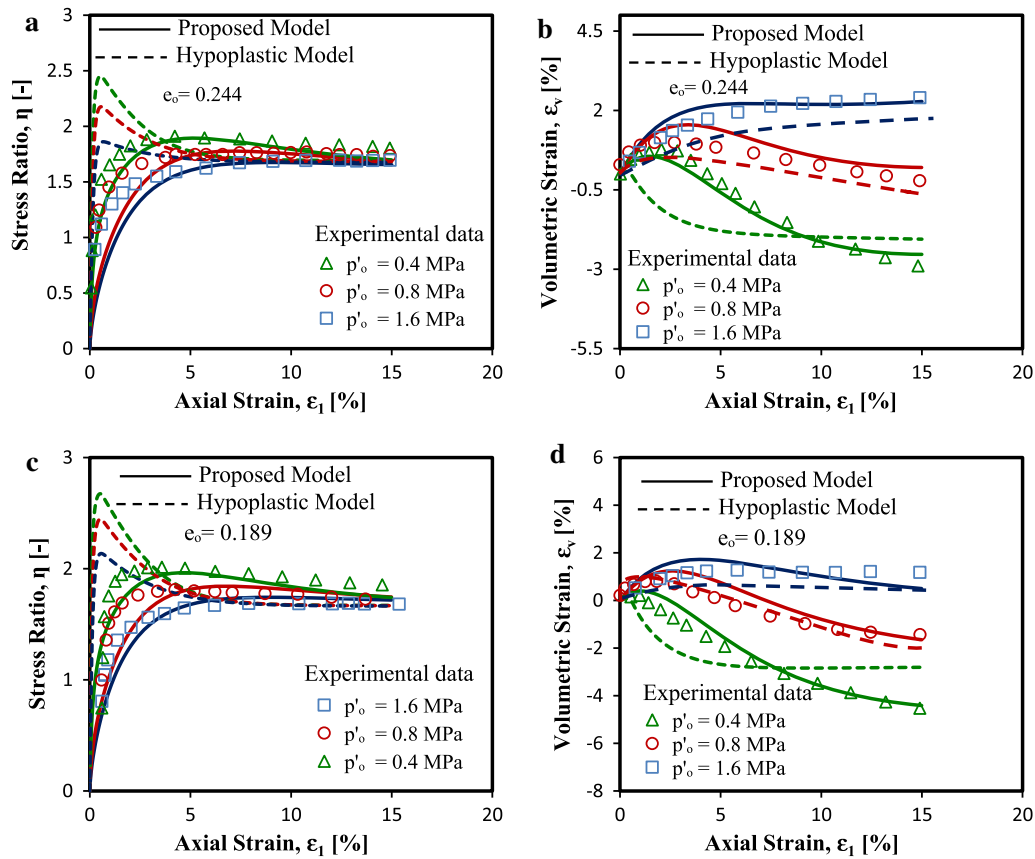


Fig. 9 The proposed and hypoplastic models predictions for mobilization of stress ratio and volume change behavior of six Tacheng rockfill specimens sheared under drained condition from $p'_o = 0.4, 0.8$ and 1.6 [MPa]: **a** and **b** three specimens with $e_0 = 0.244$; **c** and **d** three specimens with $e_0 = 0.189$ (data from [117, 119])

According to Eq. (4), v is obtained by using initial and ultimate GSDs. In the lack of ultimate grading curve, $\langle D \rangle_0^2 = D_M^2 \left(\frac{2-\varpi}{5-\varpi} \right)$ is a satisfactory assumption [e.g., Einav [22]]. The proposed range of ϖ is 2.5 to 2.8 [e.g., Sammis et al. [93]]. Otherwise, v can be derived by the calculation of the second-order moments $[\langle D \rangle^2]$ of the initial and ultimate GSDs *see* Fig. 5a]. β_1 and β_2 can be determined through a curve fitting process by using the initial and ultimate GSDs along with Eq. (2). Figure 5b demonstrates the values of β_1 and β_2 for Kurnell sand. M_c and M_e are the slopes of CSL in the q - p' plane under triaxial compression and extension, respectively. Figure 5c presents M_c for Kurnell sand. λ and e_i are the slope and the reference void ratio of the CSL in the e vs. $(p'/p_{ref})^\xi$ plane under nil particle breakage (say initial grading). On the other hand, e_u is related to the intercept of the CSL in e vs. $(p'/p_{ref})^\xi$ plane corresponding to the ultimate GSD (*see* Fig. 2). Once e_i and e_u were determined, e_T can be obtained using Eq. (18). Figure 5d represents the calculation of e_T for the Kurnell sand.

n_d can be determined using the results of monotonic undrained triaxial tests on medium-dense and dense specimens exhibiting phase transformation (i.e., certain effective stress state at which the initial contraction turns into dilation). According to Eq. (23), n_d is the slope of the best line fitted to the phase transformation data in the $\ln(M_d/M)$ vs. ψ_d plane wherein M_d and ψ_d are, respectively, the values of η and ψ at the phase transformation. Likewise, the plastic hardening modulus becomes zero at the peak shear strength in the conventional drained tests on medium-dense and dense specimens. According to Eq. (23), n_b is the slope of the best line fitted to the peak stress ratio data in the $\ln(M/M_b)$ vs. ψ_b plane wherein M_b and ψ_b are the peak stress ratio and the corresponding state parameter, respectively. Parts “e” and “f” of Fig. 5 show the determination of n_b and n_d for the Kurnell sand.

Using Eqs. (22) and (9)_a for the conventional drained triaxial compression tests ($s = +1$), the following equation can be obtained e.g., [31]:

Table 3 The hypoplastic model parameters for simulation of drained triaxial compression tests on Tacheng rockfill

$\chi = 6.0$	$n = 0.24$	$e_{c0} = 0.19$	$e_{c0} = 0.55$	$e_{i0} = 0.63$	$\alpha = 0.14$	$\beta = 3.2$	$m_T = 1.095$	$m_R = 2.19$	$R = 0.0015$
$\varphi_c = 41 [^\circ]$	$h_s = 970 [MPa]$	$\alpha_p = 0.6 [kPa^{-2}]$	$\alpha_q = 0.4 [kPa^{-2}]$	$\beta_p = 0.7 [kPa^{-1}]$	$\beta_q = 0.4 [kPa^{-1}]$	$C_{u0} = 5.54$	$\gamma_{min} = 0.029$	$\gamma_{max} = 0.017$	$B = 1.0$

$$d = \frac{\dot{\varepsilon}_v^i}{\dot{\varepsilon}_q^i} = \frac{\dot{\varepsilon}_v - \dot{\varepsilon}_v^{er}}{\dot{\varepsilon}_q - \dot{\varepsilon}_q^{er}} = \frac{\dot{\varepsilon}_v - (3G p' - J \dot{q}) / (3GK - J^2)}{\dot{\varepsilon}_q - (K \dot{q} - J p') / (3GK - J^2)}$$

$$\approx \frac{\Delta \varepsilon_v - (3G \Delta p' - J \Delta q) / (3GK - J^2)}{\Delta \varepsilon_q - (K \Delta q - J \Delta p') / (3GK - J^2)} = d_0 (M_d - \eta) \tag{32}$$

d_0 is determined using Eq. (32) for drained triaxial tests on medium-dense and dense specimens following phase transformation and prior reaching the critical state. Figure 5g presents determination of d_0 for the Kurnell sand.

h and c_h can be calculated by fitting the predicted to the q vs. ε_q curves of the undrained and drained triaxial tests covering a wide range of initial void ratios. ω manages the pace of particle breakage owing to shear loading and can be interconnected to W_q^p/e_0 through Eq. (28). Figure 5h illustrates determination of ω for the Kurnell sand.

5 The constitutive model predictive capacity

5.1 Drained and undrained monotonic and cyclic triaxial tests on Toyoura sand

Verdugo and Ishihara [106] carried out an extensive series of undrained and drained triaxial compression tests covering a wide range of initial states (i.e., $p'_0 = 0.1$ to 3.0 [MPa] and $e_0 = 0.735$ to 0.996 [–]) on Toyoura sand specimens prepared using moist tamping method. A majority of the Toyoura sand particles were made of quartz, and accordingly, no tangible sign of particle breakage within the effective stress range investigated was traced by Verdugo and Ishihara [106]. In the testing program, each specimen was isotropically consolidated to the target p'_0 value, sheared under undrained/drained condition until $\varepsilon_1 \approx 25$ [%] was reached and thereafter, unloaded to the isotropic effective stress state. Using the model parameter listed in Table 2, the model simulations for four undrained tests on dense ($e_0 = 0.735$) specimens [see parts “a” and “b”], seven undrained tests on medium-loose and loose ($e_0 = 0.833$ and 0.907) specimens [see parts “c” and “d”], and six drained tests on initially loose and very loose specimens ($e_0 = 0.810$ to 0.960) [see parts “e” and “f”] are compared to the corresponding laboratory data in Fig. 6. Without changing the model parameters for Toyoura sands, the undrained behaviors of two specimens subjected to cyclic shear from $p'_0 \approx 0.30$ [kPa] are simulated and plotted against the corresponding laboratory data in Fig. 7. As can be seen, the proposed model is capable of capturing Toyoura sand behavior subjected to both monotonic and cyclic loadings with different initial confining pressures and void ratios to a satisfactory extent. Of note, particle

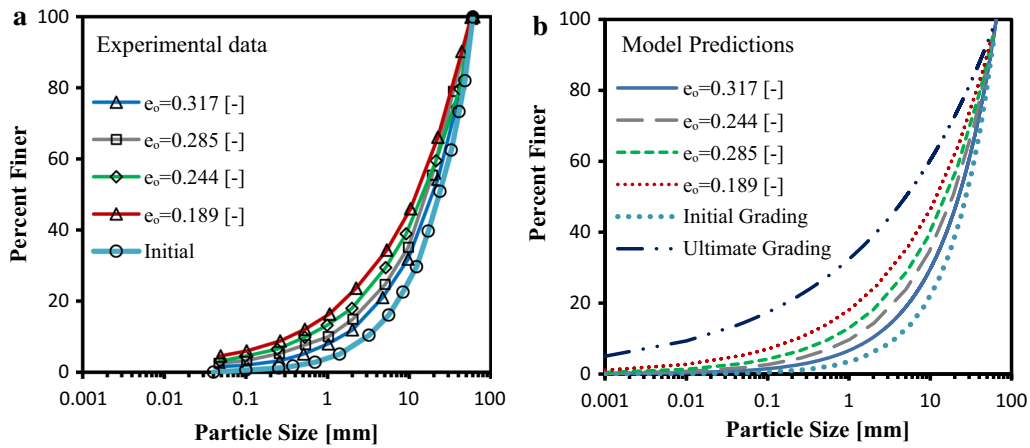


Fig. 10 Change in GSD of Tacheng rockfill material with $p'_0 = 1.6$ [MPa]: **a** experimental data, **b** the proposed model predictions (data from Xiao et al. [116])

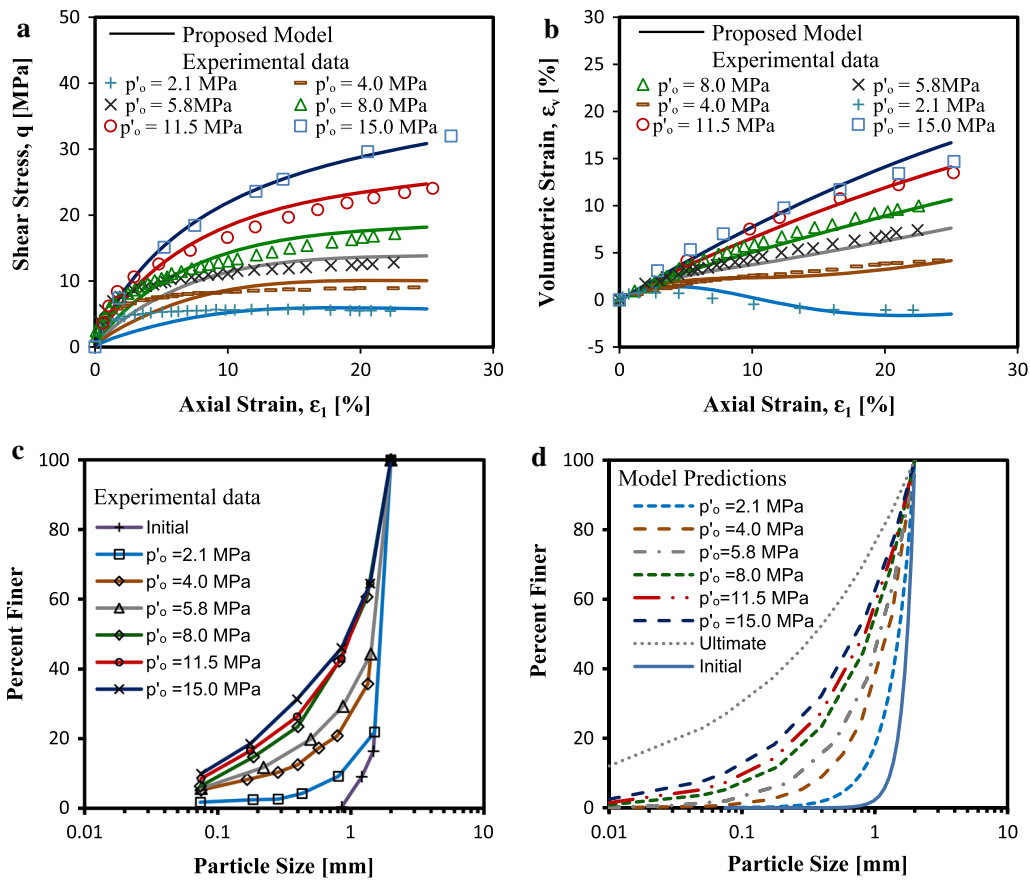


Fig. 11 The proposed model predictions for: **a** mobilization of shear strength with axial strain; **b** volume change behavior with axial strain; **c** and **d** change in GSD for six Cambria sand specimens sheared under drained condition from $p'_0 = 2.1, 4.0, 5.8, 8.0, 11.5$ and 15.0 [MPa] with $e_0 = 0.52$ (data from Yamamuro and Lade [123])

breakage for the experiments performed on Toyoura sand by Verdugo and Ishihara [106] was negligible and thus, e_i and e_u were set identical.

5.2 Drained triaxial tests on Tacheng rockfill

Tacheng rockfill collected from Shangrila County of China is a well-graded gravel with fines content of 1.8% and uniformity coefficient of 5.54 see [117, 119]. Large-scale

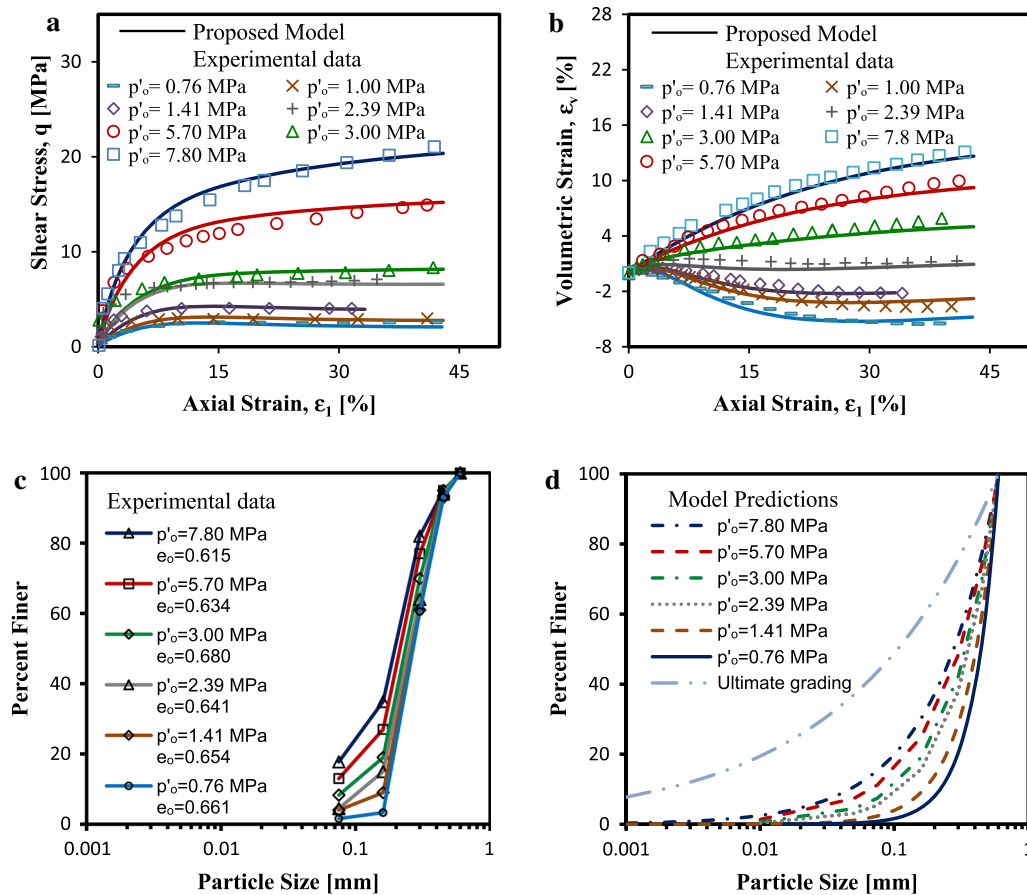


Fig. 12 The proposed model predictions for: **a** mobilization of shear strength with axial strain; **b** volume change behavior with axial strain; **c** and **d** change in GSD for six Kernell sand specimens sheared under drained condition from $p'_0 = 0.76, 1.41, 2.39, 3.0, 5.7$ and 7.8 [MPa] with $e_0 = 0.615$ to 0.680 [data from Russel and Khalili (2004)]

triaxial specimens were prepared in five consecutive layers. To form each layer, Tacheng rockfill was carefully dropped into the split mold and then compacted using a vibrator and later saturated through vacuum saturation. Specimens were consolidated isotropically under $p'_0 = 0.4, 0.8$ and 1.6 [MPa] and then sheared under conventional drained condition. In Figs. 8 and 9, the proposed model simulations obtained from the use of the model parameters listed in Table 2 for Tacheng sand are illustrated against the experimental data of initially loose to dense Tacheng rockfill reported by [117, 119]. Engin et al. [25] revised the hypoplastic model proposed by von Wolffersdorff [107] in order to improve its ability to simulate the crushable granular soils behavior (see Appendix 2). The nonlinear incremental formulation of hypoplasticity adopts neither a yield function nor decomposition of strain into elastic and plastic parts. Engin et al. [25] incorporated a history dependency into the hypoplasticity formulation to capture the effect of particle breakage. For the sake of comparison, the predicted behaviors from the hypoplastic

model are included in the figures. The model was implemented and calibrated with the parameters listed in Table 3. The Tacheng rockfill specimens exhibit more dilatative behavior when crushing is negligible under low confining stress (e.g., $p'_0 = 0.4$ [MPa]). Increase in particle breakage in Figs. 8 and 9 caused the volume change behaviors become progressively contractive. The overall behavior is well reproduced by the proposed model. On the other side, the hypoplastic model tends to overestimate the peak stress ratio and failed to predict realistically both the dilatative and contractive responses. For the drained tests carried out under $p'_0 = 1.6$ [MPa], the evolved GSDs measured at the end of the experiments (say $\epsilon_1 = 15$ [%]) are plotted against the model predictions in Fig. 10. Particle breakage led to a broadening of GSD and increased the fines content. The model in conjunction with Eq. (2) was successful to replicate the change in GSD from its initial one to those reached at the end of the tests.

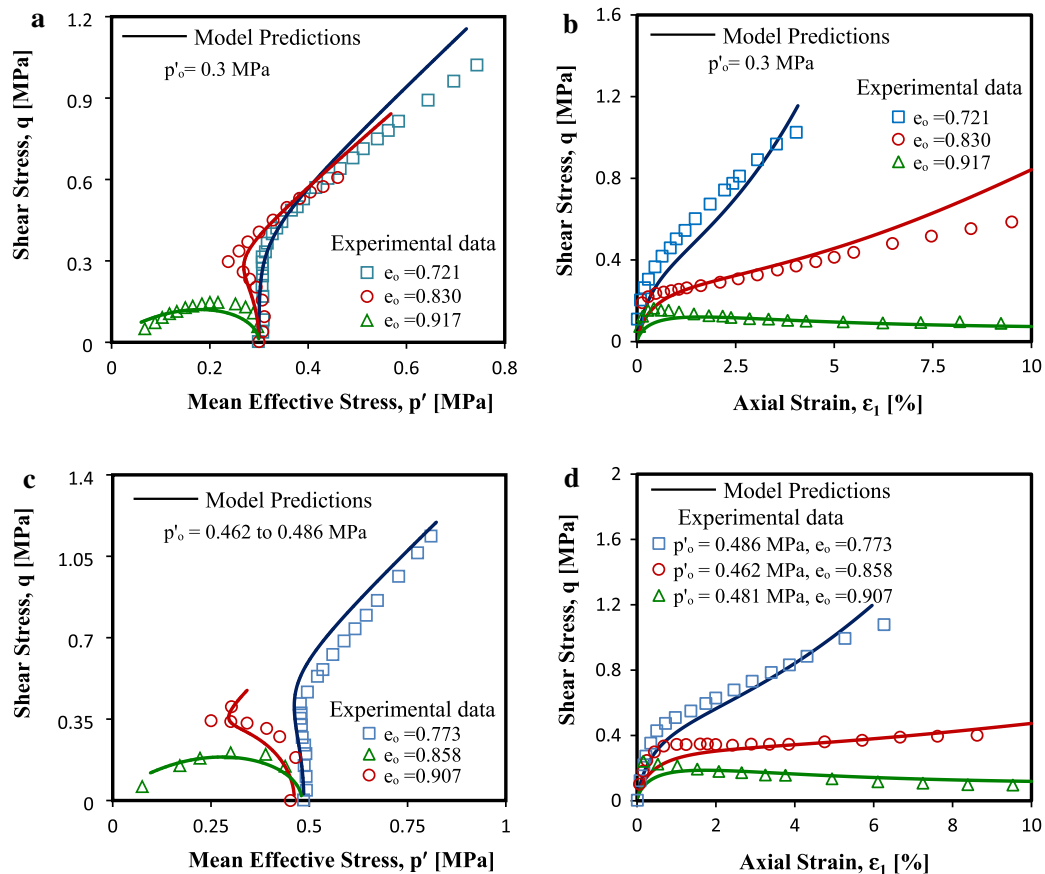


Fig. 13 The proposed model predictions for the undrained effective stress path and mobilization of shear strength with axial strain of: (a) and (b) three Kernell sand specimens with $e_0 = 0.721, 0.830,$ and 0.917 sheared from $p'_0 = 0.30$ [MPa]; (c) and (d) three Kernell sand specimens with $e_0 = 0.773, 0.858,$ and 0.907 sheared from $p'_0 = 0.462$ to 0.486 [MPa] [data from Russel and Khalili (2004)]

5.3 Drained triaxial tests on Cambria sand

Cambria sand is a uniformly graded sandy soil with sub-rounded particles covering sizes from 0.83 to 2.00 mm. Specimens for the conventional drained triaxial compression tests were prepared using dry pluviation method. For six Cambria sand specimens with $e_0=0.52$ sheared from $p'_0 = 2.1, 4.0, 5.8, 8.0, 11.5$ and 15.0 [MPa], the proposed model predictions for the mobilization of shear stress with axial strain, volumetric strain with axial strain and GSDs at the end of experiments agree reasonably with the corresponding laboratory data in Fig. 11. Of note, the model parameters used in simulations illustrated in Fig. 11 are listed in Table 2.

5.4 Drained and undrained triaxial tests on Kurnell sand

According to Russell and Khalili [91], Kurnell sand (with uniformity coefficient of 1.83 and mean particle size of 0.31 mm) is a predominantly quartz sand collected from sand dunes at Kernell, Sydney, Australia. Using the model

parameters reported in Table 2 for Kurnell sand, the mechanical behavior of six Kurnell sand specimens subjected to conventional drained shear under $p'_0 = 0.76, 1.41, 2.39, 3.0, 5.7$ and 7.8 [MPa] with $e_0 = 0.615, 0.634, 0.680, 0.641, 0.654,$ and 0.661 is plotted against their corresponding data in Fig. 12. To predict undrained behavior of six Kurnell sand specimens in Fig. 13, all model parameters except $h = 90$ [–] are considered the same as drained tests which are illustrated in Table 2. An explanation for this assumption is the fact that the strain rate and the size of the samples were different between drained and undrained tests. Moreover, enlarged lubricated end plates were used for conducting drained tests on Kurnell sand, while undrained tests were performed by using rough end plates. In Figs. 12 and 13, the proposed model shows its predictive capacity in simulation of 12 drained and undrained triaxial tests performed on sand specimens prepared through dissimilar methods within a wide range of initial void ratios and confining stresses.

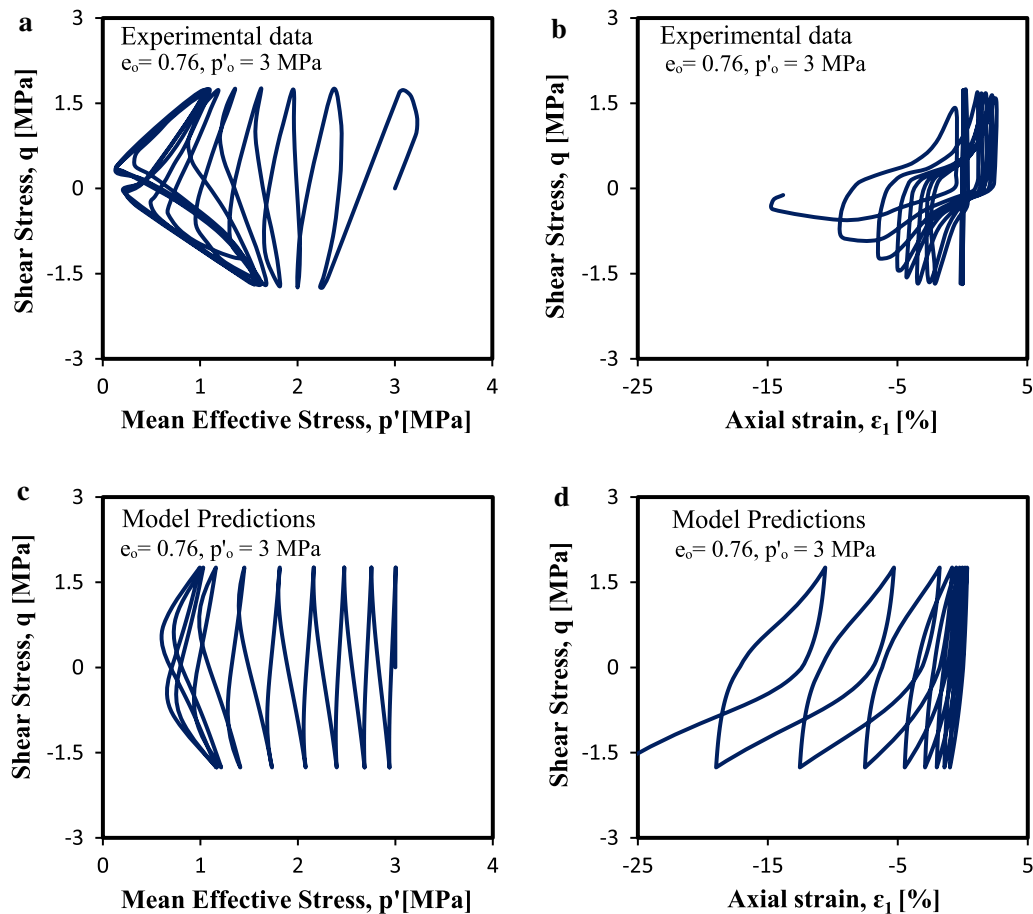


Fig. 14 The proposed model predictions for a cyclic triaxial test on an Aio sand specimen sheared under undrained condition from $p'_0 = 3$ [MPa]: **a** and **b** experimental data; **c** and **d** modified model prediction (data from Wu et al. [113])

5.5 Undrained cyclic triaxial tests on Aio sand

Aio sand (with uniformity coefficient of 2.74 and specific gravity of 2.64) collected from Yamaguchi prefecture in the south-west of Honshu Island located in Japan. Aio sand contains sub-angular to angular grains with the maximum and minimum void ratios equal to 0.958 and 0.582, respectively *see* [43, 113]. Figures 14, 15 and 16 present the undrained cyclic triaxial tests performed by Wu et al. [113] and Hyodo et al. [43] on Aio sand. Continuous pore-water pressure buildup caused reduction in the mean effective stress. Furthermore, axial strain was accumulated mainly toward the extension side. The mechanical behavior of both samples was well reproduced by the proposed constitutive model. The breakage-induced progressive downward relocation of the CSL in the e vs. p' plane causes an increase in state parameter and thereafter, a tangible decrease in plastic hardening modulus (through decrease in M^b). The presence of B as the third term in the nominator of Eq. (23)_a and the breakage-induced decrease in K_p together magnify generation of irreversible strains.

Consequently, particle breakage can affect the evolution of hysteresis loops under cyclic loads. Figure 17 demonstrates the evolution of GSD after experiments performed by Hyodo et al. [43] versus model predictions. Figure 18 presents the variation of breakage index with W_q^p/e_0 for cyclic tests performed by Hyodo et al. [43] on Aio sand. Of note, e_i and e_u for Aio sand have been determined using monotonic tests performed by Hyodo et al. [44] and cyclic tests reported by Hyodo et al. [43] and Wu et al. [113]. Regarding Figs. 14, 15 and 16, the proposed model simulations are in a satisfactory agreement with the experimental results.

6 Conclusion

In this paper, a new constitutive model able to simulate the mechanical behavior of granular materials with and without shear-induced particle breakage was proposed. The main contents are summarized as follows:

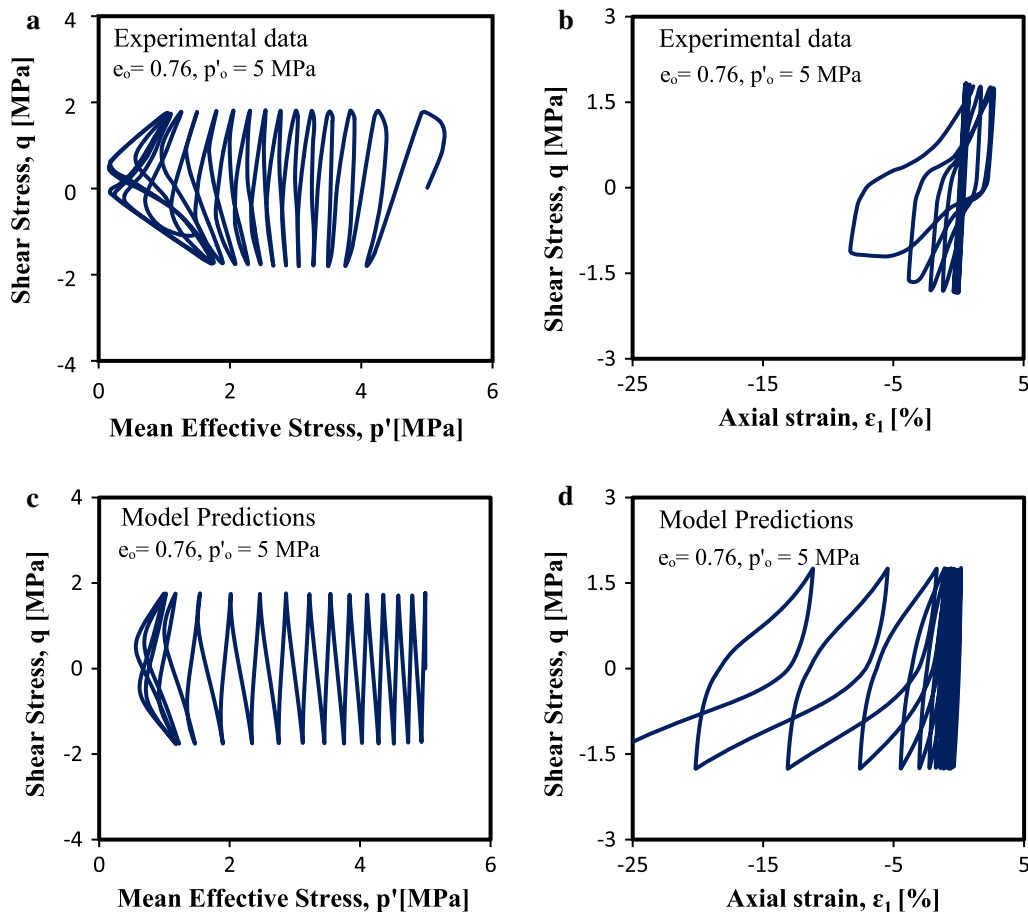


Fig. 15 The proposed model predictions for a cyclic triaxial test on an Aio sand specimen sheared under undrained condition from: **a** and **b** experimental data; **c** and **d** modified model prediction (data from Wu et al. [113])

- The hyperelastic strain rates were driven based on a generalized Jiang and Liu-type Helmholtz free energy function to guarantee the reversibility of the elastic strains. In order to account for the effect of particle breakage and coupling between plastic strains and hyperelastic properties, an additional hyperelastic-plastic coupling variable was incorporated into the Helmholtz free energy function.
- A breakage index evolving with the plastic shear work was employed to quantify shear-induced particle breakage and to play the role of elastic-plastic coupling variable. It was realized that the plastic work overestimates the shear-induced particle breakage in loose sands. However, it was shown that a reasonable correspondence between the shear-induced plastic shear work normalized by the initial void ratio and shear-induced breakage exists. By relating the breakage index to a kinematic hardening parameter, coupling emerged into the formulation. This makes the pressure-dependent moduli evolve as a function of the hardening variable.
- The numerical analyses are performed for a series of triaxial tests on both materials with permanent grains as well as with grain crushing. The comparisons indicate that the established model is applicable to capture stress-strain behavior of granular materials over a wide range of initial void ratios and confining pressures with the same set of model constants. Both the monotonic and cyclic loading have been considered.
- A hypoplastic model is used for comparison purposes. Comparisons revealed a discrepancy between predictions and experimental data considering the peak stress ratio and the dilatancy with the same set of material parameters.

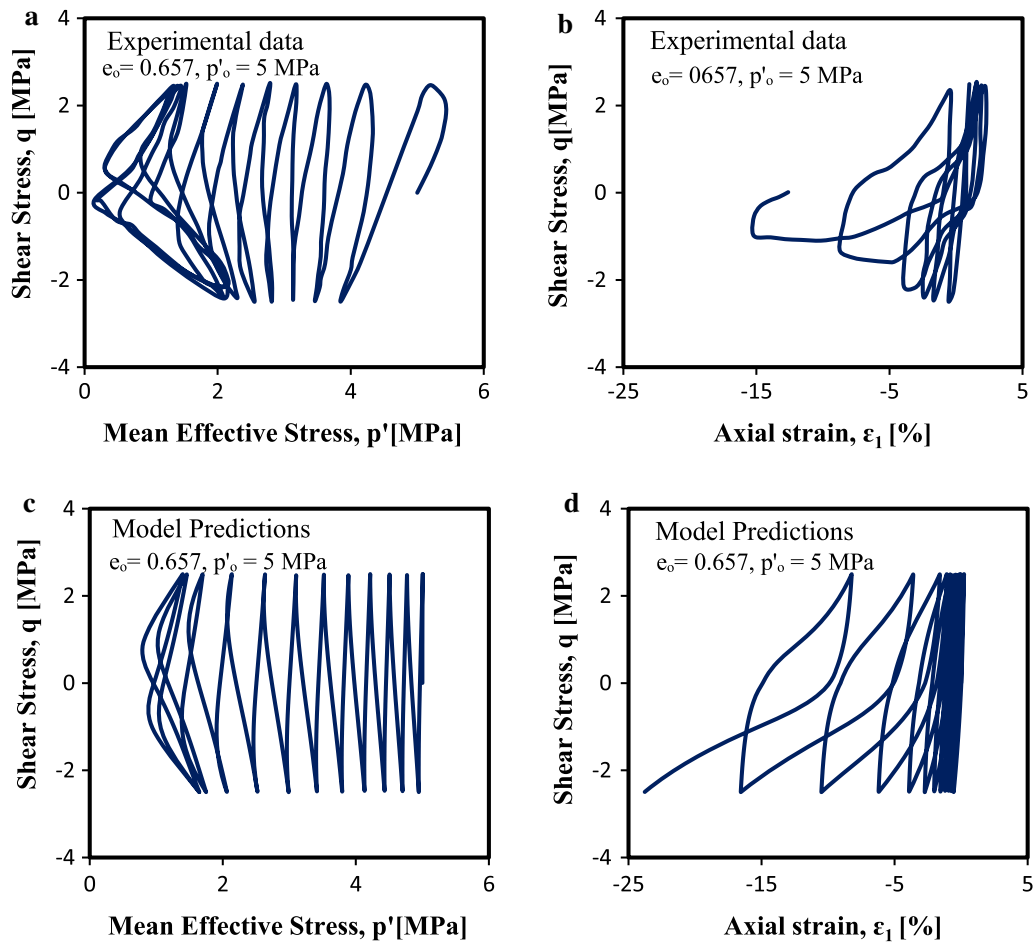


Fig. 16 The proposed model predictions for a cyclic triaxial test on an Aio sand specimen sheared under undrained condition from: **a** and **b** experimental data; **c** and **d** modified model prediction (data from Hyodo et al. [43])

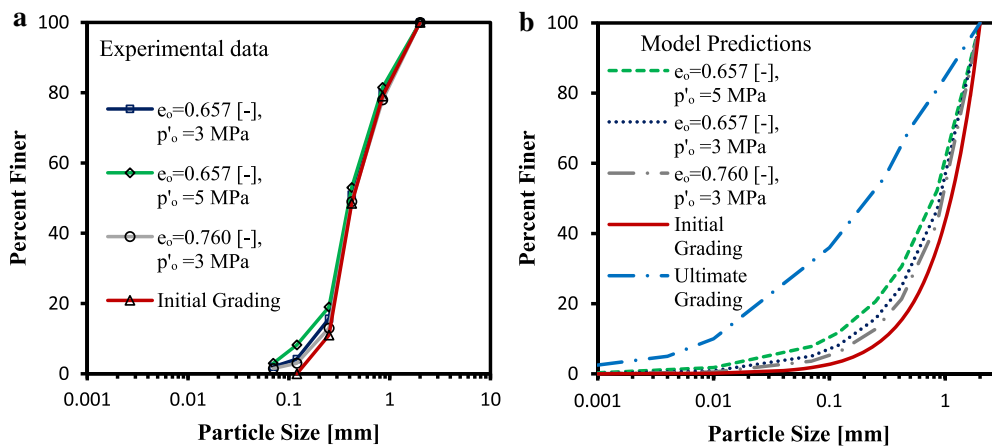


Fig. 17 Change in GSD of Aio sand: **a** experimental data **b** the proposed model predictions (data from Hyodo et al. [43] and Wu et al. [113])

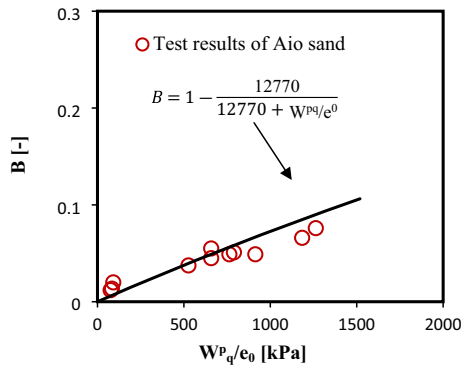


Fig. 18 Variation of breakage index for Aio sand with W_q^p/e_0 (data from Hyodo et al. [43])

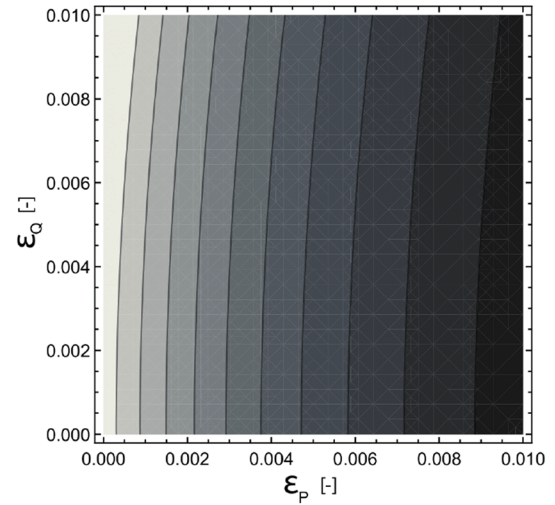


Fig. 20 Contours of constant elastic strain components using Tacheng rockfill model constants

Appendices

Appendix 1. Evaluation of the hyperelastic formulation

One of the main advantages of employing a hyperelastic formulation is the energy conservative framework for any arbitrary closed-loop effective stress path. To bring an example in this regard, the closed stress cycle presented in

Fig. 19a has been simulated. By considering the behavior as purely elastic, the elastic strain components are calculated using Eqs.7 and 14. $G_0 = 50$, $K_0 = 0.75G_0$, $\chi = 0.95$, and $\nu = 0.6$ have been assumed for the numerical simulations. In Fig. 19b–d, closed loops have been obtained for

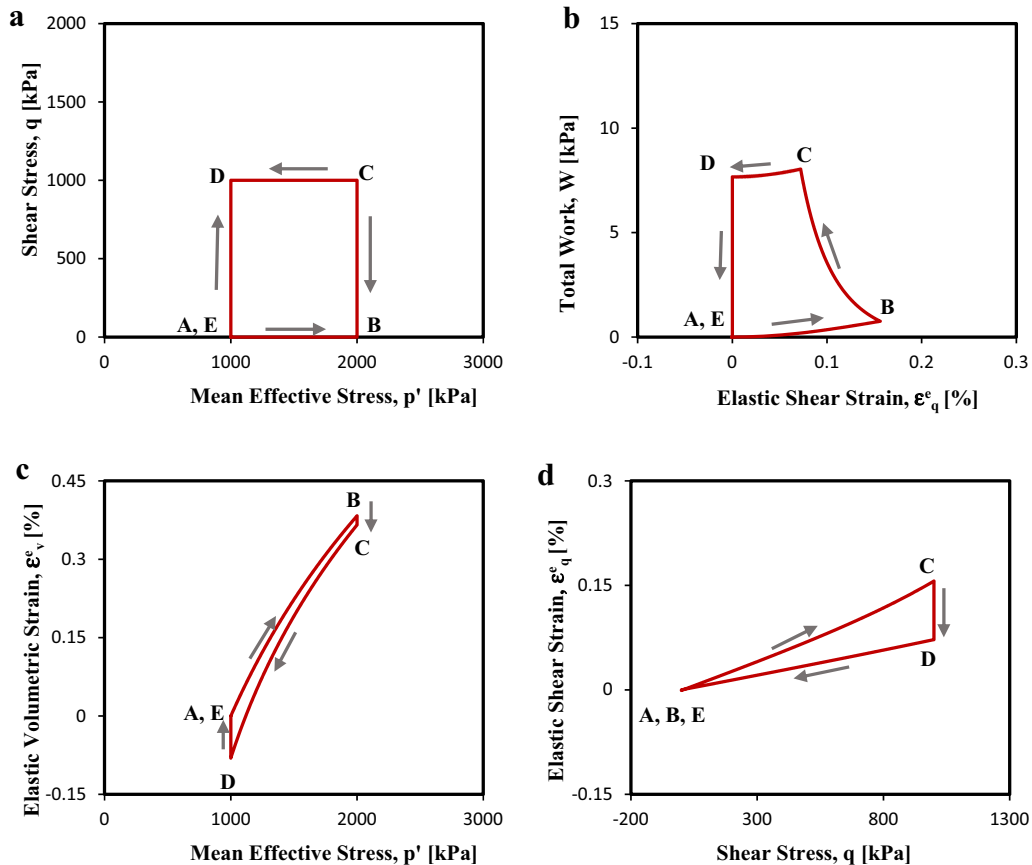


Fig. 19 Response of the hyperelaastic constitutive equations in a closed-loop purely elastic stress path **a**: effective stress path, **b**: stored work versus elastic shear strain, **c**: elastic volumetric strain versus mean effective stress, and **d**: elastic shear strain versus shear stress

both the strains and the total work, which is positive for the assumed stress path. It should be noted that changing the sense of the rotation (say $E \rightarrow D \rightarrow C \rightarrow B \rightarrow A$ instead of $A \rightarrow B \rightarrow C \rightarrow D \rightarrow E$) does not affect the magnitude of elastic strain components. In order to further evaluate the elastic part of the model, the contours of constant elastic strain proposed by Houlsby et al. [37] have been used. The suggested graphic depicts isolines ($\varepsilon_p = \sqrt{3}/3 \varepsilon_v = \text{constant}$; $\varepsilon_Q = 3/2 \varepsilon_q = \text{constant}$) in the isomorphic strain space. Figure 20 demonstrates such isolines for the proposed model. Unlike isotropic elasticity, the deviatoric portion of stress affects the isotropic portion of strain and vice versa. Such an anisotropic response makes the contours of constant ε_p and ε_Q to be curved. Apart the well-known advantages of the hyperelasticity, this framework imposes mathematical requirements which should be fulfilled. In the development of hyperelastic frameworks, the elastic stiffness should fulfill the following equations [42]:

$$\begin{aligned} K &\geq 0 \\ 3G &\geq 0 \\ 3GK - J^2 &\geq 0 \end{aligned} \quad (33)$$

These requirements render the following relation, which should be fulfilled by the herein proposed model:

$$\frac{K_0}{G_0} \leq \frac{3}{2\gamma\eta^2} \quad (34)$$

The above equation should be considered for the calibration of the elastic parameters.

Appendix 2: A hypoplastic model for crushable granular soils [25]

The model has been developed as an improved version of the grain crushing hypoplastic model of Rohe [89], which is based on the hypoplastic model by von Wolffersdorff [107]. The basic hypoplastic model can be described by a nonlinear tensorial equation as:

$$\dot{\sigma}' = \mathcal{L} : \dot{\varepsilon} + \mathbf{N} \|\dot{\varepsilon}\| \quad (35)$$

wherein σ and ε are effective stress and strain tensors, respectively. The fourth-order tensor \mathcal{L} and the second-order tensor \mathbf{N} are, respectively, associated with the linear and nonlinear parts of the behavior. Both \mathcal{L} and \mathbf{N} are functions of effective stress and strain rate tensors. In general, in the hypoplastic framework, neither the definition of a yield surface nor a decomposition of strain rates is necessary. Furthermore, the nonlinear irreversible strains are defined by means of the degree of nonlinearity and the flow rule. Here, only the enhancement of Engin et al. [25] will be summarized. The attentive reader is referred to the cited references for further details about hypoplasticity.

Given the fact that grain crushing is irreversible, Engin et al. [25] the reference void ratios at the densest state, critical state, and loosest states, respectively, through:

$$\begin{aligned} e_{d0}^* &= e_{\min}^0 - \Delta e_{\min}^{\text{ref}}; e_{c0}^* = e_{\max}^0 - \Delta e_{\max}^{\text{ref}}; e_{i0}^* \\ &= e_i^0 - \frac{e_i^0}{e_{\max}^0} \Delta e_{\max}^{\text{ref}} \end{aligned} \quad (36)$$

with:

$$\Delta e_x^{\text{ref}} = \gamma_x \ln \frac{C_{u0} + \alpha_p p_m'^2 + \alpha_q q_m'^2 - \beta_p p_m' - \beta_q q_m'}{C_{u0}} \quad (37)$$

The subscript x denotes either minimum or maximum void ratio modification. In Eqs. (36) and (37), α_p , α_q , β_p , β_q , C_{u0} , γ_{\min} , and γ_{\max} are model parameters.

Funding Open Access funding enabled and organized by Projekt DEAL.

Open Access This article is licensed under a Creative Commons Attribution 4.0 International License, which permits use, sharing, adaptation, distribution and reproduction in any medium or format, as long as you give appropriate credit to the original author(s) and the source, provide a link to the Creative Commons licence, and indicate if changes were made. The images or other third party material in this article are included in the article's Creative Commons licence, unless indicated otherwise in a credit line to the material. If material is not included in the article's Creative Commons licence and your intended use is not permitted by statutory regulation or exceeds the permitted use, you will need to obtain permission directly from the copyright holder. To view a copy of this licence, visit <http://creativecommons.org/licenses/by/4.0/>.

References

- Alonso EE, Olivella S, Pinyol NM (2005) A review of Beliche Dam. *Géotechnique* 55(4):267–285
- Ashkar Z, Lashkari A (2014) A hyperelastic theory for granular soils and its application. In: 2nd Iranian Conference on Geotechnical Engineering, Iran
- Bandini V, Coop MR (2011) The influence of particle breakage on the location of the critical state line of sands. *Soils Found* 51(4):591–600
- Been K, Jefferies MG (1985) A state parameter for sands. *Géotechnique* 35(2):99–112
- Borja RI, Tamagnini C, Amorosi A (1997) Coupling plasticity and energy-conserving elasticity models for clays. *J Geotech Geoenviron Eng* 123(10):948–957
- Carraro JAH, Prezzi M, Salgado R (2009) Shear strength and stiffness of sands containing plastic or nonplastic fines. *J Geotech Geoenviron Eng* 135(9):1167–1178
- Charles JA, Watts KS (1980) The influence of confining pressure on the shear strength of compacted rockfill. *Géotechnique* 30(4):353–367
- Chávez C, Alonso EE (2003) A constitutive model for crushed granular aggregates which includes suction effects. *Soils Found* 43(4):215–227

9. Chen X, Zhang J (2016) Effect of load duration on particle breakage and dilative behavior of residual soil. *J Geotech Geoenviron Eng* 142(9):06016008
10. Ciantia MO, Arroyo M, O'Sullivan C, Gens A, Liu T (2019) Grading evolution and critical state in a discrete numerical model of Fontainebleau sand. *Géotechnique* 69(1):1–15
11. Cil MB, Alshibli KA (2014) 3D evolution of sand fracture under 1D compression. *Géotechnique* 64(5):351–364
12. Cil MB, Hurley RC, Graham-Brady L (2020) Constitutive model for brittle granular materials considering competition between breakage and dilation. *J Eng Mech* 146(1):04019110
13. Collins IF, Housley GT (1997) Application of thermomechanical principles to the modelling of geotechnical materials. *Proc R Soc London* 453(1964):1975–2001
14. Collins-Craft NA, Stefanou I, Sulem J, Einav I (2020) A Cosserat breakage mechanics model for brittle granular media. *J Mech Phys Solids* 2:103975
15. Coop MR, Sorensen KK, Bodas Freitas T, Georgoutsos G (2004) Particle breakage during shearing of a carbonate sand. *Géotechnique* 54(3):157–163
16. Dafalias YF, Manzari MT (2004) Simple plasticity sand model accounting for fabric change effects. *J Eng Mech* 130(6):622–634
17. Dai B, Yang J, Luo X (2015) A numerical analysis of the shear behavior of granular soil with fines. *Particuology* 21:160–172
18. Daouadji A, Hicher PY, Rahma A (2001) An elastoplastic model for granular materials taking into account grain breakage. *Eur J Mech A Solids* 20:113–137
19. Daouadji A, Hicher PY (2010) An enhanced constitutive model for crushable granular materials. *Int J Numer Anal Meth Geomech* 34(6):555–580
20. de Bono J, McDowell G (2016) Particle breakage criteria in discrete-element modelling. *Géotechnique* 66(12):1014–1027
21. Donohue S, O'sullivan C, Long M (2009) Particle breakage during cyclic triaxial loading of a carbonate sand. *Géotechnique* 59(5):477–482
22. Einav I (2007) Breakage mechanics—part I: theory. *J Mech Phys Solids* 55(6):1274–1297
23. Einav I (2007) Breakage mechanics—Part II: modelling granular materials. *J Mech Phys Solids* 55(6):1298–1320
24. Einav I, Puzrin AM (2004) Pressure-dependent elasticity and energy conservation in elastoplastic models for soils. *J Geotech Geoenviron Eng* 130(1):81–92
25. Engin HK, Jostad HP, Rohe A (2014) On the modelling of grain crushing in hypoplasticity. In: *proceedings of conference on numerical methods in geotechnical engineering*, pp 33–38
26. Fraszny RJ, Voss ME (1986) Undrained compression behavior of sand. *J Geotech Eng* 112(3):334–347
27. Frossard E, Hu W, Dano C, Hicher PY (2012) Rockfill shear strength evaluation: a rational method based on size effects. *Géotechnique* 62(5):415–427
28. Gajo A, Bigoni D, Wood DM (2001). Stress induced elastic anisotropy and strain localisation in sand. In: *Bifurcation and localisation theory in geomechanics*, pp 37–44
29. Gajo A, Bigoni D (2008) A model for stress and plastic strain induced nonlinear, hyperelastic anisotropy in soils. *Int J Numer Anal Meth Geomech* 32(7):833–861
30. Ghafghazi M, Shuttle DA, DeJong JT (2014) Particle breakage and the critical state of sand. *Soils Found* 54(3):451–461
31. Golchin A, Lashkari A (2014) A critical state sand model with elastic–plastic coupling. *Int J Solids Struct* 51(15–16):2807–2825
32. Graham J, Housley GT (1983) Anisotropic elasticity of a natural clay. *Géotechnique* 33(2):165–180
33. Guo WL, Zhu JG (2017) Particle breakage energy and stress dilatancy in drained shear of rockfills. *Géotechnique Lett* 7(4):304–308
34. Hagerty MM, Hite DR, Ullrich CR, Hagerty DJ (1993) One-dimensional high-pressure compression of granular media. *J Geotech Eng* 119(1):1–18
35. Hardin BO (1985) Crushing of soil particles. *J Geotech Eng* 111(10):1177–1192
36. Hardin BO, Richart FE (1963) Elastic wave velocities in granular soils. *ASCE J Soil Mech Found Div* 89(1):33–65
37. Housley GT, Amorosi A, Rojas E (2005) Elastic moduli of soils dependent on pressure: a hyperelastic formulation. *Géotechnique* 55(5):383–392
38. Housley GT, Amorosi A, Rollo F (2019) Non-linear anisotropic hyperelasticity for granular materials. *Comput Geotech* 115:103167
39. Hu W, Yin Z, Dano C, Hicher PY (2011) A constitutive model for granular materials considering grain breakage. *Sci China Technol Sci* 54(8):2188–2196
40. Hueckel T (1976) Coupling of elastic and plastic deformations of bulk solids. *Meccanica* 11(4):227–235
41. Hueckel T, Maier G (1977) Incremental boundary value problems in the presence of coupling of elastic and plastic deformations: a rock mechanics oriented theory. *Int J Solids Struct* 13(1):1–15
42. Humrickhouse PW, Sharpe JP, Corradini ML (2010) Comparison of hyperelastic models for granular materials. *Phys Rev E* 81(1):011303
43. Hyodo M, Wu Y, Aramaki N, Nakata Y (2017) Undrained monotonic and cyclic shear response and particle crushing of silica sand at low and high pressures. *Can Geotech J* 54(2):207–218
44. Hyodo M, Hyde AFL, Aramaki N, Nakata Y (2002) Undrained monotonic and cyclic shear behaviour of sand under low and high confining stresses. *Soils Found* 42(3):63–76
45. Indraratna B, Ionescu D, Christie HD (1998) Shear behavior of railway ballast based on large-scale triaxial tests. *J Geotech Geoenviron Eng* 124(5):439–449
46. Indraratna B, Wijewardena LSS, Balasubramaniam AS (1993) Large-scale triaxial testing of grey wacke rockfill. *Géotechnique* 43(1):37–51
47. Indraratna B, Salim W (2002) Modelling of particle breakage of coarse aggregates incorporating strength and dilatancy. *Proc Inst Civ Eng-Geotech Eng* 155(4):243–252
48. Indraratna B, Sun QD, Nimbalkar S (2015) Observed and predicted behaviour of rail ballast under monotonic loading capturing particle breakage. *Can Geotech J* 52(1):73–86
49. Ishihara K, Tatsuoka F, Yasuda S (1975) Undrained deformation and liquefaction of sand under cyclic stress. *Soils Found* 15(1):29–44
50. Ishihara K, Towhata I (1983) Sand response to cyclic rotation of principal stress directions as induced by wave loads. *Soils Found* 23(4):11–26
51. Iwasaki T, Tatsuoka F (1977) Effects of grain size and grading on dynamic shear moduli of sands. *Soils Found* 17(3):19–35
52. Jiang Y, Liu M (2003) Granular elasticity without the Coulomb condition. *Phys Rev Lett* 91(14):144301
53. Jia Y, Xu B, Chi S, Xiang B, Zhou Y (2017) Research on the particle breakage of rockfill materials during triaxial tests. *Int J Geomech* 17(10):04017085
54. Jia Y, Xu B, Chi S, Xiang B, Xiao D, Zhou Y (2019) Particle breakage of rockfill material during triaxial tests under complex stress paths. *Int J Geomech* 19(12):04019124
55. Karatza Z, Andò E, Papanicolopoulos SA, Viggiani G, Ooi JY (2019) Effect of particle morphology and contacts on particle

- breakage in a granular assembly studied using X-ray tomography. *Granul Matter* 21(3):1–13
56. Kementzetzidis E, Corciulo S, Versteijlen WG, Pisano F (2019) Geotechnical aspects of offshore wind turbine dynamics from 3d non-linear soil-structure simulations. *Soil Dyn Earthq Eng* 120:181–199
 57. Kikumoto M, Wood DM, Russell A (2010) Particle crushing and deformation behaviour. *Soils Found* 50(4):547–563
 58. Koseki J, Kawakami S, Nagayama H, Sato T (2000) Change of small strain quasi-elastic deformation properties during undrained cyclic torsional shear and triaxial tests of Toyoura sand. *Soils Found* 40(3):101–110
 59. Lade PV, Yamamuro JA, Bopp PA (1996) Significance of particle crushing in granular materials. *J Geotech Eng* 122(4):309–316
 60. Lashkari A (2010) A SANISAND model with anisotropic elasticity. *Soil Dyn Earthq Eng* 30(12):1462–1477
 61. Lashkari A (2014) Recommendations for extension and re-calibration of an existing sand constitutive model taking into account varying non-plastic fines content. *Soil Dyn Earthq Eng* 61–62:212–238
 62. Lashkari A, Falsafizadeh SR, Shourijeh PT, Alipour MJ (2020) Instability of loose sand in constant volume direct simple shear tests in relation to particle shape. *Acta Geotech* 15:2507–2527
 63. Lashkari A, Latifi M (2008) A non-coaxial constitutive model for sand deformation under rotation of principal stress axes. *Int J Num Anal Methods Geomech* 32:1051–1086
 64. Lashkari A, Yaghtin MS (2018) Sand flow liquefaction instability under shear-volume coupled strain paths. *Géotechnique* 68(11):1002–1024
 65. Lee KL, Farhoomand I (1967) Compressibility and crushing of granular soil in anisotropic triaxial compression. *Can Geotech J* 4(1):68–86
 66. Lee J, Salgado R, Carraro JAH (2004) Stiffness degradation and shear strength of silty sands. *Can Geotech J* 41(5):831–843
 67. Leslie DD (1963) Large scale triaxial tests on gravelly soils. In: *Proceedings of the 2nd Pan-American conference on SMFE, Brazil, vol 1, pp 181–202*
 68. Leung CF, Lee FH, Yet NS (1997) The role of particle breakage in pile creep in sand. *Can Geotech J* 33(6):888–898
 69. Liu H, Zou D, Liu J (2014) Constitutive modeling of dense gravelly soils subjected to cyclic loading. *Int J Numer Anal Meth Geomech* 38(14):1503–1518
 70. Liu HY, Abell JA, Diambra A, Pisano F (2019) Modelling the cyclic ratcheting of sands through memory-enhanced bounding surface plasticity. *Geotechnique* 69(9):783–800
 71. Macháček J, Staubach P, Tafili M, Zachert H, Wichtmann T (2021) Investigation of three sophisticated constitutive soil models: From numerical formulations to element tests and the analysis of vibratory pile driving tests. *Comput Geotech* 1(138):104276
 72. Mao W, Towhata I (2015) Monitoring of single-particle fragmentation process under static loading using acoustic emission. *Appl Acoust* 94:39–45
 73. Mao W, Yang Y, Lin W, Aoyama S, Towhata I (2018) High frequency acoustic emissions observed during model pile penetration in sand and implications for particle breakage behavior. *Int J Geomech* 18(11):04018143
 74. McDowell GR, Bolton MD (1998) On the micromechanics of crushable aggregates. *Géotechnique* 48(5):667–679
 75. Minh NH, Cheng YP (2013) A DEM investigation of the effect of particle-size distribution on one-dimensional compression. *Géotechnique* 63(1):44–53
 76. Miura N, Yamanouchi T (1975) Effect of water on the behavior of a quartz-rich sand under high stresses. *Soils Found* 15(4):23–34
 77. Miura N, Sukeo O (1979) Particle-crushing of a decomposed granite soil under shear stresses. *Soils Found* 19(3):1–14
 78. Muir Wood D, Maeda K (2008) Changing grading of soil: effect on critical states. *Acta Geotech* 3(1):3–14
 79. Mun W, McCartney JS (2017) Roles of particle breakage and drainage in the isotropic compression of sand to high pressures. *J Geotech Geoenviron Eng* 143(10):04017071
 80. Nakata Y, Kato Y, Hyodo M, Hyde AF, Murata H (2001) One-dimensional compression behaviour of uniformly graded sand related to single particle crushing strength. *Soils Found* 41(2):39–51
 81. Nguyen GD, Einav I (2009) The energetics of cataclasis based on breakage mechanics. *Pure Appl Geophys* 166(10–11):1693–1724
 82. Norouzi N, Lashkari (2021) An anisotropic critical state plasticity model with stress ratio-dependent fabric tensor. *Iranian J Sci Tech* 45:2577–2594
 83. Okada Y, Sassa K, Fukuoka H (2004) Excess pore pressure and grain crushing of sands by means of undrained and naturally drained ring-shear tests. *Eng Geol* 75(3–4):325–343
 84. Ovalle C (2020) Hicher PY (2020) Modeling the effect of wetting on the mechanical behavior of crushable granular materials. *Geosci Front* 11(2):487–494
 85. Papamichos E, Vardoulakis I, Ouadfel H (1993) Permeability reduction due to grain crushing around a perforation. *Int J Rock Mech Min Sci Geomech Abstr* 30(7):1223–1229
 86. Pestana JM, Whittle A (1995) Compression model for cohesionless soils. *Géotechnique* 45(4):611–632
 87. Salgado R, Bandini P, Karim A (2000) Shear strength and stiffness of silty sand. *J Geotech Geoenviron Eng* 126(5):451–462
 88. Rahman MdM, Lo SR, Baki MdAL (2011) Equivalent granular state parameter and undrained behavior of sand-fine mixtures. *Acta Geotech* 6:183–194
 89. Rohe A (2010) On the modelling of grain crushing in hypoplasticity. Technical report, TUDelft
 90. Rubin MB, Einav I (2011) A large deformation breakage model of granular materials including porosity and inelastic distortional deformation rate. *Int J Eng Sci* 49(10):1151–1169
 91. Russell AR, Khalili N (2004) A bounding surface plasticity model for sands exhibiting particle crushing. *Can Geotech J* 41(6):1179–1192
 92. Sammis CG, Osborne RH, Anderson JL, Banerdt M, White P (1986) Self-similar cataclasis in the formation of fault gouge. *Pure Appl Geophys* 124(1):53–78
 93. Sazzad MM, Suzuki K (2013) Density dependent macro-micro behavior of granular materials in general triaxial loading for varying intermediate principal stress using DEM. *Granul Matter* 15(5):583–593
 94. Shahnazari H, Rezvani R, Tutunchian MA (2017) Experimental study on the phase transformation point of crushable and non-crushable soils. *Mar Georesour Geotechnol* 35(2):176–185
 95. Tafili M, Wichtmann T, Triantafyllidis T (2021) Experimental investigation and constitutive modeling of the behaviour of highly plastic Lower Rhine Clay under monotonic and cyclic loading. *Can Geot J*. <https://doi.org/10.1139/cgj-2020-0012>
 96. Tafili M, Triantafyllidis T (2020) A simple hypoplastic model with loading surface accounting for viscous and fabric effects of clays. *Int J Numer Anal Meth Geomech* 44(16):2189–2215
 97. Tafili M, Triantafyllidis T (2020) AVISA: anisotropic visco-ISA model and its performance at cyclic loading. *Acta Geotech*. <https://doi.org/10.1007/s11440-020-00925-9>
 98. Tafili M, Triantafyllidis T (2020) Cyclic and monotonic response of silts and clays: experimental analysis and constitutive modelling. *Eur J Environ Civ Eng*. <https://doi.org/10.1080/19648189.2020.1734096>

99. Tafili M, Triantafyllidis T (2020d) State-dependent dilatancy of soils: experimental evidence and constitutive modeling. In: book: Recent developments of soil mechanics and geotechnics in theory and practice. https://doi.org/10.1007/978-3-030-28516-6_4
100. Taiebat M, Dafalias YF (2008) SANISAND: Simple anisotropic sand plasticity model. *Int J Numer Anal Meth Geomech* 32(8):915–948
101. Tengattini A, Das A, Einav I (2016) A constitutive modelling framework predicting critical state in sand undergoing crushing and dilation. *Géotechnique* 66(9):695–710
102. Thevanayagam S, Shenthana T, Mohan S, Liang J (2002) Undrained fragility of clean sands, silty sands, and sandy silts. *ASCE J Geotech Geoenviron Eng* 128(10):849–859
103. Timpong S, Miura S, Yara K (2005) Effect of consolidation time on shear modulus of crushable volcanic soils. *Soils Found* 45(5):115–119
104. Ueng TS, Chen TJ (2000) Energy aspects of particle breakage in drained shear of sands. *Géotechnique* 50(1):65–72
105. Varadarajan A, Sharma KG, Venkatachalam K, Gupta AK (2003) Testing and modeling two rockfill materials. *J Geotech Geoenviron Eng* 129(3):206–218
106. Verdugo R, Ishihara K (1996) The steady state of sandy soils. *Soils Found* 36(2):81–91
107. Von Wolffersdorff PA (1996) A hypoplastic relation for granular materials with a predefined limit state surface. *Mech Cohesive-Frict Mater* 1(3):251–271
108. Wang JJ, Zhang HP, Tang SC, Liang Y (2013) Effects of particle size distribution on shear strength of accumulation soil. *J Geotech Geoenviron Eng* 139(11):1994–1997
109. Wang Z, Wang G, Ye Q (2020) A constitutive model for crushable sands involving compression and shear induced particle breakage. *Comput Geotech* 126:103757
110. Wichtmann T, Triantafyllidis T (2009) Influence of the grain-size distribution curve of quartz sand on the small strain shear modulus G_{max} . *J Geotech Geoenviron Eng* 135(10):1404–1418
111. Wichtmann T, Triantafyllidis T (2018) Monotonic and cyclic tests on kaolin: a database for the development, calibration and verification of constitutive models for cohesive soils with focus to cyclic loading. *Acta Geotech* 13(5):1103–1128
112. Wei H, Li X, Zhang S, Zhao T, Yin M, Meng Q (2021) Influence of particle breakage on drained shear strength of calcareous sands. *Int J Geomech* 21(7):04021118
113. Wu Y, Hyodo M, Aramaki N (2018) Undrained cyclic shear characteristics and crushing behaviour of silica sand. *Geomech Eng* 14(1):1–8
114. Xiao Y, Liu H, Chen Y, Chu J (2014) Strength and dilatancy of silty sand. *J Geotech Geoenviron Eng* 140(7):06014007
115. Xiao Y, Liu H, Yang G, Chen Y, Jiang J (2014) A constitutive model for the state-dependent behaviors of rockfill material considering particle breakage. *Sci China Technol Sci* 57(8):1636–1646
116. Xiao Y, Liu H, Chen Y, Jiang J (2014) Strength and deformation of rockfill material based on large-scale triaxial compression tests. II: influence of particle breakage. *J Geotech Geoenviron Eng* 140(12):04014071
117. Xiao Y, Liu H, Ding X, Chen Y, Jiang J, Zhang W (2016) Influence of particle breakage on critical state line of rockfill material. *Int J Geomech* 16(1):04015031
118. Xiao Y, Liu H, Chen Q, Ma Q, Xiang Y, Zheng Y (2017) Particle breakage and deformation of carbonate sands with wide range of densities during compression loading process. *Acta Geotech* 12(5):1177–1184
119. Xiao Y, Liu H, Desai CS, Sun Y, Liu H (2016) Effect of intermediate principal-stress ratio on particle breakage of rockfill material. *J Geotech Geoenviron Eng* 142(4):06015017
120. Xiao Y, Liu H (2017) Elastoplastic constitutive model for rockfill materials considering particle breakage. *Int J Geomech* 17(1):04016041
121. Xiao Y, Yuan Z, Chu J, Liu H, Huang J, Luo SN, Wang S, Lin J (2019) Particle breakage and energy dissipation of carbonate sands under quasi-static and dynamic compression. *Acta Geotech* 14(6):1741–1755
122. Yamamuro JA, Bopp PA, Lade PV (1996) One-dimensional compression of sands at high pressures. *J Geotech Eng* 122(2):147–154
123. Yamamuro JA, Lade PV (1996) Drained sand behavior in axisymmetric tests at high pressures. *J Geotech Eng* 122(2):109–119
124. Yang J, Sze HE (2011) Cyclic behavior and resistance of saturated sand under non-symmetrical loading conditions. *Géotechnique* 61(1):59–73
125. Yang J, Wei LM (2012) Collapse of loose sand with the addition of fines: the role of particle shape. *Géotechnique* 62(12):1111–1125
126. Yu FW (2017) Particle breakage and the critical state of sands. *Géotechnique* 67(8):713–719
127. Yu F (2018) Particle breakage and the undrained shear behavior of sands. *Int J Geomech* 18(7):04018079
128. Yu F (2018) Particle breakage in triaxial shear of a coral sand. *Soils Found* 58(4):866–880
129. Zhang S, Tong CX, Li X, Sheng D (2015) A new method for studying the evolution of particle breakage. *Géotechnique* 65(11):911–922

Publisher's Note Springer Nature remains neutral with regard to jurisdictional claims in published maps and institutional affiliations.